# Homer condensates orchestrate YAP-Wnt signaling crosstalk downstream of the Crumbs polarity complex

Siti Maryam J M Yatim[1,2], Linda Jiabao Woo[1,2], Yuhong Chen[1,2], Barbara Hübner[1,2], and Alexander Ludwig[1,2,#]

[1] School of Biological Sciences, Nanyang Technological University Singapore, 60 Nanyang Drive, Singapore 637551
[2] NTU Institute of Structural Biology, Nanyang Technological University Singapore, 59 Nanyang Drive, Singapore 636921

[#] correspondence: aludwig@ntu.edu.sg

## Abstract
The Hippo pathway controls cell growth, proliferation and differentiation, and is frequently deregulated in cancers. YAP, the central transcriptional co-activator of the Hippo pathway, is suppressed by the canonical Hippo kinases and several poorly characterized non-canonical mechanisms. YAP also interacts with the Wnt/β-catenin signaling pathway, yet how this crosstalk is regulated is not well understood. Here we show that Homer scaffolding proteins act downstream of the Crumbs polarity complex to promote YAP/TEAD and canonical Wnt/β-catenin signaling in epithelial and cancer cells. We demonstrate that Homers via their EVH1 domains interact directly with the Crumbs complex protein PatJ as well as with the NDR kinase scaffolding protein Furry-like (FRYL). FRYL acts antagonistically to Homers in controlling YAP/TEAD signaling but cooperates with Homers to promote Wnt/β-catenin signaling output. Intriguingly, live and fixed cell imaging, Fluorescence Recovery After Photobleaching, and electron microscopy revealed that all three Homer proteins form cytoplasmic biomolecular condensates with unique ultrastructural and material properties. These condensates effectively sequestered PatJ, FRYL, NDR, YAP, and β-catenin, with PatJ and FRYL exerting opposing effects on the condensate's properties. Finally, in colorectal cancer cells, Homers enhance YAP and Wnt signaling and promote cell migration, suggesting a tumor-promoting function for Homers. Overall, our findings suggest that Homers coordinate YAP-Wnt signaling crosstalk through cytoplasmic phase separation, linking polarity cues to transcriptional regulation.

## Introduction
The Hippo pathway controls cell growth, proliferation, differentiation and survival, and is deregulated in many cancers. At the heart of this pathway are the transcriptional coactivators Yes-associated protein (YAP) and its paralogue Transcriptional co-activator with PDZ-binding motif (TAZ, also known as WWTR1), which shuttle between the cytoplasm and the nucleus. Nuclear import of YAP/TAZ is controlled by the canonical Hippo core kinase cassette, which is composed of the Ste20-like kinases 1/2 (MST1/2) and Large Tumor Suppressor 1/2 (LATS1/2) kinases. LATS1/2 phosphorylate YAP/TAZ on several serine/threonine residues, resulting in the retention of YAP/TAZ in the cytoplasm or in proteasome-mediated degradation via 14-3-3 proteins. The ensuing omission of YAP/TAZ from the nucleus suppresses YAP target gene expression via TEA domain transcription factors (TEADs) [1, 2]. Apart from the canonical Hippo kinase cascade, several other kinases have been shown to regulate YAP including MST3 and MST4 [3], the LATS-related kinases NDR1/2 [4, 5], and MAP4K and MEKK [2]. These kinases are controlled by a plethora of signals including the actin cytoskeleton, extracellular matrix stiffness, cell shape and cell polarity, and cell-cell junction assembly. How such diverse signals are sensed and integrated to regulate Hippo pathway output is not clear.

YAP signaling is closely intertwined with other signaling pathways including the TGFβ, NOTCH, and Wnt pathways [6, 7, 8, 9, 10]. Several studies have demonstrated that YAP/TAZ play a dual role in regulating Wnt/β-catenin signaling [11, 12, 13, 14, 15]. In the absence of a Wnt signal, cytoplasmic YAP/TAZ are incorporated into the β-catenin destruction complex via an interaction with Axin1 to promote β-catenin degradation [12]. However, when Wnt signaling is activated, YAP/TAZ dissociate from the destruction complex and translocate into the nucleus to form transcriptional complexes with β-catenin and the TCF/LEF transcription factors, leading to the expression of YAP/TAZ and Wnt-dependent target genes [12, 15]. YAP/TAZ may also suppress Wnt signaling by binding to Disheveled, which prevents its activation [11], or by binding directly to β-catenin, which stabilizes β-catenin in the cytoplasm [14]. Moreover, both canonical and non-canonical Wnt signaling mechanisms can feedback to the Hippo pathway to control the activity of YAP [16, 17]. Such complex reciprocal interactions between the YAP/TAZ and Wnt pathways have significant implications during differentiation, regeneration, and in cancers [18, 19, 20], yet how this pathway crosstalk is regulated is not well understood.

The epithelial Crumbs complex, which is composed of the transmembrane protein Crumbs (Crb), the cytoplasmic adaptor protein Pals1, and the multi-PDZ domain scaffolding protein PatJ, is an evolutionarily conserved and important upstream regulator of the Hippo pathway [21, 22, 23, 24, 25]. *Drosophila* Crb suppresses cell and tissue growth by promoting YAP/TAZ retention at apical cell membranes [26, 27, 28, 29]. Loss of Crb3 or Pals1 in mammalian cell culture models and in mice also causes hyperactivation of YAP/TAZ as well as defects in tissue organization and differentiation [30, 31, 32, 33]. However, the signaling mechanisms that connect the Crumbs complex to the Hippo/YAP pathway remain poorly characterized, especially in mammalian systems.

We previously demonstrated that the mammalian Crumbs complex defines a distinct cortical domain apical of epithelial tight junctions, which we termed the vertebrate marginal zone (VMZ) [23, 34]. In that study we also identified the Homer scaffolding proteins as novel interactors of PatJ. All three Homer paralogues expressed in mammals (Homer1, 2, and 3) are composed of an N-terminal EVH1 domain, which connects Homers to various ligands containing consensus PPxxF motifs, and a C-terminal coiled coil domain, which mediates homo and hetero-oligomerisation [35, 36, 37]. Homers are well known for their roles as postsynaptic scaffolding proteins and have been implicated in calcium signaling, receptor trafficking, and the control of postsynaptic actin organization. However, their roles in non-neuronal tissues are largely unexplored.

Here we show that Homers link the Crumbs complex to a non-canonical signaling pathway that controls YAP-Wnt signaling crosstalk. Loss and gain of function approaches coupled with imaging, transcriptomics, qPCR, and reporter assays showed that Homers promote YAP/TEAD and canonical Wnt pathway activity in MDCK, 293T, and HCT116 colorectal cancer cells. We further demonstrate that Homers directly interact with and inhibit a FRYL/NDR kinase complex, which suppresses YAP/TEAD activity but promotes Wnt signaling. Interestingly, Homers exert their functions through the formation of cytoplasmic biomolecular condensates, which exhibit unique material characteristics and efficiently sequester PatJ, FRYL/NDR, YAP, and β-catenin. Altogether our data indicate that Homer condensates regulate YAP-Wnt signaling crosstalk in cancer and non-cancer cells.

## Results

### PatJ directly interacts with and recruits Homers to apical cell junctions

Homers are highly expressed in the brain but are also detected in various non-neuronal tissues including the heart, lung, intestine, and kidney [38]. Using proximity proteomics and

expression of GFP-tagged Homer proteins we previously demonstrated that all Homers localize to the apical-lateral border in fully polarized Madin Darby Canine Kidney type II (MDCK-II) cells. To verify this, we performed immunofluorescence confocal microscopy of MDCK monolayers using specific antibodies against Homers (Fig 1A), which confirmed that all endogenous Homers localize to apical cell junctions. Moreover, antibodies against Homer1, which is the only Homer protein expressed in the kidney [38], produced an apical junctional and punctate cytoplasmic staining in mouse kidney sections that partially colocalized with the tight junction marker ZO-1 (Fig 1B-1D) (Pearson's R = 0.60 ± 0.08; n=30). We concluded that Homers are an integral component of apical cell junctions in renal epithelial cells.

We previously demonstrated an interaction between PatJ and Homers using co-immunoprecipitations (co-IPs) [34]. PatJ is a large PDZ-domain containing protein that has been shown to interact with the Hippo pathway regulators angiomotin (AMOT) and KIBRA [23, 39, 40, 41]. In addition, PatJ connects the Crumbs complex to the tight junction proteins claudin-1 and ZO-1 or ZO-3 [23, 42, 43]. To understand the mechanistic basis of the Homer/PatJ interaction, we screened the PatJ protein sequence for PPxxF motifs that might provide docking sites for the Homer EVH1 domains. Two highly conserved PxxF motifs were identified in PatJ (Fig 2A). One of which (PPPF) is located at the C-terminus of the PDZ4 domain, the other (PKGF) in the linker region between PDZ5 and PDZ6. To test whether these motifs are required for the interaction with Homers, we transfected GFP tagged PatJ PDZ domain constructs into 293T cells (Fig 2B). All GFP-PDZ domain fragments were immunoprecipitated using anti-GFP antibodies followed by Western blotting against Homers endogenously expressed in 293T cells. The analysis demonstrated that PDZ5-6 of PatJ was sufficient to co-IP Homer1, Homer2, and Homer3 from 293T cell lysates. By contrast, PDZ3-4 did not interact with Homers (Fig 2C). Mutation of the conserved PKGF motif (into AKGA) in the PDZ5-6 construct (Fig 2C) or in full-length PatJ (PatJ1-8) (Fig 2D) abolished the binding to Homers in co-IPs. Moreover, mutation of glycine 89 (G89) in the Homer1 EVH1 domain, which is essential for ligand binding [44], abolished the interaction with PatJ (Fig 2E) and interfered with the recruitment of Homers to cell-cell junctions in MDCK cells (not shown). Interestingly, the Homer1 EVH1 domain alone was insufficient to interact with PatJ in IP experiments (Fig 2F), suggesting that Homer oligomerization via the coiled-coil domains is required for a stable interaction with PatJ. To test whether PatJ oligomerizes with Homers, we performed sucrose density gradient centrifugation on 293T cell lysates derived from GFP- or GFP-PatJ1-8-transfected cells. Indeed, GFP-PatJ1-8 partially co-fractionated with Homer1 in the gradient and markedly increased the size or density of Homer1 oligomers compared to control-transfected cells (Fig 2G). We concluded that PatJ interacts directly with the EVH1 domain of Homers via a conserved PxxF motif located in the linker between PDZ domains 5 and 6 to assemble higher order PatJ/Homer hetero-oligomers.

To test whether PatJ is required for the recruitment of Homers to the apical-lateral border, we co-cultured MDCK wild-type (WT) and PatJ knockout (KO) cells on Transwell filters and stained such co-cultures with antibodies against each Homer protein. Antibodies against Pals1, which is lost from apical cell junctions in the absence of PatJ [45], were used to discriminate between WT and PatJ KO cells. In WT cells, all Homers localized to the apical-lateral border, as expected. By contrast, in cells lacking PatJ, all Homer proteins were clearly displaced from apical cell junctions (Fig 2H and 2I). Western blotting showed that the expression of Homers was not notably altered in PatJ KO cells (Fig 2J). We concluded that PatJ is essential for the recruitment of Homers to apical cell junctions.

**Homers promote YAP/TEAD and Wnt signaling in MDCK-II and 293T cells**

To address the functions of individual Homers and the entire Homer protein family, we generated single and triple MDCK Homer KO cells using CRISPR/Cas9 gene editing. All KO

lines were validated by PCR/DNA sequencing of the guide RNA target locus, Western blotting, and immunofluorescence (Fig S1A-S1F). Single Homer KO cells and Homer triple KO (TKO) cells grew normally and showed no obvious defects in cell proliferation or epithelial polarization (data now shown). In addition, the localization of PatJ and Pals1, the tight junction proteins ZO-1 and occludin, and the adherens junction protein β-catenin was unaffected in Homer TKO cells (Fig S1G). This indicates that Homers are dispensable for cell polarity development and the assembly and maintenance of the apical junctional complex.

We hypothesized, therefore, that Homers may play a signaling rather than a structural role at apical cell junctions. To test this, we analysed the transcriptome of Homer TKO cells using RNA sequencing (Fig S2A, Table S2). Interestingly, genes involved in cancer signaling including transcriptional regulators, metabolic enzymes, ion channels and transporters, and RhoGTPase regulators were significantly deregulated in Homer TKO cells (Fig 3A, 3B and Fig S2B). Closer inspection of the differentially expressed genes (DEGs) showed that the canonical YAP/TEAD target genes CTGF, ANKRD1 and GADD45A [46] were downregulated in Homer TKO cells (Fig 3C). Other potential YAP/TEAD target genes including FOLR2 [47], COL12A1 [48, 49], and HOXA2 [50] were downregulated as well, and so was RASSF1, an important regulator of the Hippo pathway. In addition, the expression of several genes involved in Wnt signaling was reduced in Homer TKO cells (Fig 3C). This includes the Wnt receptor FZD4, the Wnt target genes HAS2 [51, 52, 53, 54], ARHGAP24 [55], and POU3F3 [56], and GAS1 [57], DACH1 [58, 59, 60], PLEKHA4 [61], and GNA14 [62].

To verify the transcriptional changes observed by RNA sequencing, we performed qPCRs. In addition, TEAD (8xGTIIC) and TCF/LEF (TOPFlash) luciferase reporter assays were used to analyse Hippo/YAP and canonical Wnt/β-catenin pathway activity, respectively. As expected, TEAD reporter activity and the expression of CTGF and ANKRD1 was significantly reduced in Homer TKO cells (Fig 3E and 3F). Homer TKO cells also showed a 1.2-1.5-fold increase in YAP S127 phosphorylation (Fig 3D), indicating a suppression of YAP activation. qPCR analysis further confirmed that FZD4, GNA14, DACH1, and HAS2 were significantly downregulated in Homer TKO cells (Fig 3G). In addition, although the expression of the canonical Wnt target gene Axin2 was unchanged (Fig 3H), TOPFlash reporter assays showed that Wnt pathway activity was significantly reduced in Homer TKO cells (Fig 3I).

To explore whether Homers regulate YAP and Wnt signaling in non-polarized epithelial cells, we downregulated or overexpressed Homers in Human Embryonic Kidney (HEK) 293T cells, a commonly used cell line for the analysis of YAP and Wnt signaling. In agreement with our MDCK KO data, siRNA-mediated downregulation of individual or all three Homers in 293T cells reduced YAP target gene transcription (Fig 3J and Fig S3) and overexpression of Homer2 or Homer3 in 293T cells increased TEAD reporter activity (Fig 3K). Downregulation of all three Homers in 293T cells also reduced TOPFlash reporter activity (Fig 3L), whereas overexpression of Homers enhanced it (Fig 3M). Altogether the data indicated that Homers promote YAP and Wnt signaling in polarized and non-polarized epithelial cells to control the expression of a subset of YAP and Wnt pathway target genes and regulators.

Next, we asked whether the three Homer proteins expressed in MDCK cells function in a unique or redundant fashion. Intriguingly, and in stark contrast to Homer TKO cells, inactivation of *Homer1* or *Homer2* in MDCK cells resulted in a significant increase in TEAD reporter activity and YAP target gene expression (Fig S2C and S2D). By contrast, *Homer3* KO cells showed a decrease in YAP/TEAD activity, which was accompanied by an increase in YAP S127 phosphorylation (Fig S2E). In addition, overexpression of Homer3 (but not Homer1) in MDCK cells elevated TEAD and TOPFlash reporter activity (Fig S2F-S2H). This indicates that – at least in MDCK cells – Homer3 acts in a dominant fashion to promote YAP and Wnt signaling.

**Homers control YAP signaling via the NDR kinase scaffolding protein FRYL**

To understand how Homers regulate YAP/Wnt signaling downstream of the Crumbs complex, we performed immunoprecipitation-mass spectrometry (IP-MS) of GFP tagged Homer3 stably expressed in MDCK cells (Fig S4). As expected, Homer1 and Homer2 as well as PatJ were present in Homer3 IPs. We further identified the Furry-like protein (FRYL) as a novel Homer3 interacting protein. Furry is a conserved scaffolding protein of NDR1/2 kinases (Tricornered in *Drosophila*). Both Furry and NDR1/2 have been shown to regulate YAP [4, 5] and are critical for vertebrate [63] and invertebrate [64, 65, 66, 67, 68] development. FRYL may also interact with NDR1 [69] (Fig 4A), but its role in YAP signaling is unknown.

We noted that the C-terminus of FRYL harbors two PxxF motifs (PSPF and PTVF) (Fig 4B). To test whether Homers interact with FRYL via these motifs, we performed IP experiments in 293T cells transfected with full-length wild-type GFP-FRYL or two FRYL mutants (M1 and M2) in which the PxxF motifs were mutated (Homer binding mutants; HBMs). All Homer proteins co-immunoprecipitated with wild-type FRYL but not with the FRYL HBMs (Fig 4C). In addition, Homers did not co-immunoprecipitate with Furry (not shown), indicating that Homers interact directly and specifically with FRYL via their EVH1 domains. To explore a potential role of FRYL in YAP signaling, we produced *FRYL* MDCK KO cells. Loss of FRYL reduced YAP S127 phosphorylation (Fig 4D) and increased TEAD reporter activity (Fig 4E) in at least one out of the two KO clones examined. Notably, YAP nuclear translocation and YAP target gene transcription were significantly increased in both FRYL KO clones (Fig 4F and 4G), indicating that FRYL suppresses YAP/TEAD signaling. By contrast, the expression of the Wnt-associated genes FZD4, GNA14, DACH1 and HAS2 was reduced in *FRYL* KO cells (Fig 4H). Axin2 mRNA levels were also decreased but Wnt reporter activity was unexpectedly unchanged (Fig 4I and 4J). We concluded that Homers and FRYL function antagonistically in regulating the transcription of canonical YAP/TEAD target genes but synergize to control the expression of a subset of Wnt target genes and Wnt pathway regulators, possibly through distinct signaling mechanisms.

Given the opposing effects of Homers and FRYL on YAP/TEAD signaling, we hypothesized that Homers suppress the FRYL/NDR complex to enhance YAP/TEAD signaling. To test this, we first confirmed that FRYL indeed interacts with and regulates NDR1. In agreement with previous work [69], FRYL and the NDR scaffolding protein MOB1a co-immunoprecipitated with GFP-NDR1 transiently transfected in 293T cells (Fig 4K). By contrast, LATS1 was not detected in GFP-NDR1 IPs, indicating a specific interaction between FRYL and NDR1. In addition, overexpression of wild-type FRYL increased NDR Thr442/Thr444 phosphorylation (a readout for NDR activity) but did not affect the phosphorylation levels of LATS1/2 (Thr1029) (Fig 4L). This indicates that FRYL specifically promotes NDR phosphorylation, likely by promoting the association of MST kinases with NDR [70, 71]. To test whether Homers regulate the signaling output of the FRYL/NDR complex, we overexpressed FRYL or the FRYL HBM M2 in 293T cells and performed TEAD reporter assays. Interestingly, overexpression of wild-type FRYL reduced TEAD reporter activity, and this inhibitory effect was significantly enhanced when the Homer binding site in FRYL was inactivated (Fig 4M). Finally, and in agreement with the *FRYL* KO data, siRNA-mediated downregulation of FRYL in 293T cells increased YAP target gene transcription (Fig 4N). Taken together the data suggest that Homers promote YAP/TEAD signaling by suppressing the activity of the FRYL/NDR kinase complex.

**Homers are scaffolds for the formation of cytoplasmic biomolecular condensates**

To address how Homers regulate YAP/TEAD signaling, we analysed their subcellular localization in 293T cells. Intriguingly, overexpression of individual GFP-tagged Homers produced cytoplasmic puncta reminiscent of biomolecular condensates (Fig 5A).

Overexpression of wild-type FRYL, but not the FRYL HBM, resulted in the formation of similar structures (Fig 5B). Biomolecular condensates are defined as membrane-less organelles that concentrate macromolecules via multivalent interactions, generating liquid-like or gel-like compartments that vary in how readily they exchange materials with the surrounding environment [72, 73]. To ascertain that Homers indeed phase separate, we first analysed the localization of endogenous Homers using specific antibodies. All antibodies produced a punctate staining in the cytoplasm, although such endogenous Homer puncta were much smaller than the ones observed upon Homer overexpression (Fig 5C). Previous work demonstrated that macromolecular crowding induced by hyperosmotic stress promotes the phase separation of Hippo kinases and regulators of Hippo signaling [74, 75]. To test whether hyperosmotic stress enhances the phase separation behavior of endogenous Homers, we treated 293T cells for 30 or 90 min with 0.4M sorbitol. Indeed, sorbitol treatment significantly increased the size and number of endogenous cytoplasmic Homer puncta (Fig 5D), suggesting that Homers phase separate when expressed at physiological levels.

To understand when and how Homer condensates form, 293T cells were transfected with GFP-tagged Homer1, 2, or 3 and imaged live starting 6 hours post-transfection using spinning disk microscopy. At early time points of transfection, GFP-Homers showed a diffuse cytoplasmic localization (Fig 5E, 7.5 hrs, insets). Soon after, small cytoplasmic puncta started to appear (Fig 5E, 8 hrs), which grew rapidly and then coalesced or fused into larger condensates (Fig 5E, 8.5 hrs onwards, Movies S1-S3). Interestingly, whilst Homer1 condensates appeared to relax into spherical objects upon fusion, Homer2 and Homer3 condensates coalesced but did not seem to fuse (Fig 5F, Movies S4-S6). Inspection of live cells 12-16 hours post-transfection confirmed that Homer1 formed well-isolated and globular condensates throughout the cytoplasm, whereas Homer3 and particularly Homer2 condensates frequently appeared as large perinuclear clusters (Fig S5A). These observations prompted us to examine the ultrastructure of Homer condensates by transmission electron microscopy (TEM). To specifically identify Homer condensates in TEM, we expressed Homers as APEX2 fusion proteins [76, 77]. Inspection of TEM sections showed that Homer condensates are not surrounded by membranes, as expected for a phase-separated compartment (Fig 5G and Fig S5B). In line with our light microscopy data, Homer1 condensates appeared as individual spherical objects in the cytoplasm, whereas Homer2 (and to a lesser extent Homer3) condensates frequently exhibited a multi-lobal architecture, again indicating that individual condensates had coalesced but not entirely fused. Moreover, whilst Homer1 and Homer2 condensates appeared electron-dense with a smooth surface, Homer3 condensates appeared more loosely organized and often exhibited a “grainy” ultrastructure with irregular edges. Consistent with this, quantification revealed a significant difference in circularity between Homer1 and Homer2/Homer3 condensates, whereas the size of the condensates was similar (Fig 5H). We concluded that the three Homer proteins produce cytoplasmic condensates with distinct dynamic and ultrastructural properties.

Our ultrastructural analysis suggested potential differences in the material properties of Homer condensates. To test this, we analysed the mobility of GFP-tagged Homers inside the condensates using Fluorescence Recovery After Photobleaching (FRAP). We found that only ~13-26% of Homer fluorescence recovered within 1 min upon photobleaching (Fig 5I and Fig S6B). This indicated that Homers are largely immobile within the condensates, suggesting that Homer condensates are viscous, gel-like compartments. Interestingly, however, Homer1 was significantly more mobile than Homer2, with Homer3 showing intermediate levels of mobility. Taken together, live cell imaging, TEM and FRAP all indicated that Homer1 forms “droplet-like” condensates that are relatively fluid, whereas Homer2 and Homer3 condensates exhibit “gel-like” properties with more limited molecular mobility and a reduced propensity of fusion and content mixing.

**Homers recruit FRYL, NDR, YAP, β-catenin, and PatJ into biomolecular condensates**

Having established that Homers phase separate in the cytoplasm, we asked whether such condensates sequester FRYL, NDR, YAP, and β-catenin. To this end, we analysed the colocalization between Homers and these four potential client proteins in co-transfected 293T cells using confocal microscopy, line scans, and Pearson's correlation analysis (see Fig S6A for Pearson's R values). In addition, we performed FRAP to measure the mobility of each client protein inside the condensates and to assess whether the recruitment of the client alters the mobility of Homers (see Fig S6B for FRAP kinetics). We found that GFP-FRYL efficiently colocalised with condensates formed by HA-tagged Homer1 (Fig 6A). By contrast, the GFP tagged FRYL HBM was not detected in Homer1 condensates and instead was diffusely localized in the cell cytoplasm (Fig 6B). In addition, overexpression of GFP-FRYL alone was sufficient to recruit endogenous Homer1 into condensates (Fig 6C). Quantification revealed that Homers and FRYL colocalized efficiently and that colocalization was significantly reduced for the FRYL HBM (Fig 6D). We further found that Homer1 condensates were significantly larger in cells co-transfected with wild-type FRYL compared to cells co-transfected with the FRYL HBM (Fig 6D). This indicated that the Homer binding site in FRYL is not only critical for the recruitment of FRYL into Homer condensates but also suggested a role for FRYL in regulating condensate growth or assembly. To test this, we measured the mobility of mCherry-Homer3 in cells co-transfected with wild-type or mutant FRYL. Intriguingly, co-transfection of wild-type GFP-FRYL significantly increased the mobile fraction of Homer3 from ~25% to ~36% compared to cells co-transfected with the GFP-FRYL HBM (Fig 6E and Fig S6B). The fluorescence of GFP-FRYL did not recover significantly within 1 min of photobleaching (~10% mobile fraction, Fig S6B), suggesting that FRYL is firmly embedded in the condensates. We concluded that Homers recruit FRYL into cytoplasmic condensates via an EVH1-PxxF motif interaction and that FRYL regulates the condensates' material properties.

We then analysed YAP, NDR1 and β-catenin. In line with a signaling role of Homer condensates, GFP-NDR1 (Fig 6F), YAP-GFP (Fig 6G), and β-catenin-GFP (Fig 6H) all colocalized efficiently with Homer condensates in fixed cells. Interestingly, FRAP analysis demonstrated that YAP-GFP fluorescence recovered rapidly and efficiently, reaching ~76% recovery within ~15 sec upon photobleaching (Fig 6I and Fig S6B). With a fluorescence recovery of ~50%, β-catenin-GFP was also relatively mobile within the condensates (Fig 6J and Fig S6B). Co-transfection of YAP or β-catenin did not markedly alter the mobility of Homer3 compared to cells transfected with Homer3 alone (compare Fig 6I and 6J with Fig 5H, and see Fig S6B). We concluded that Homer condensates efficiently sequester FRYL, NDR, YAP, and β-catenin to regulate YAP/TEAD and Wnt/β-catenin signaling.

Next, we analysed the localization and signaling function of PatJ. As expected, the GFP-PatJ5-6 fragment, which is sufficient for binding to PatJ (Fig 2C), co-localized with condensates containing mCherry-Homer3 and endogenous YAP (Fig 7A). FRAP measurements of cells co-transfected with GFP-PatJ5-6 and mCherry-Homer3 revealed that ~60% of GFP-PatJ5-6 fluorescence recovered within ~20 sec of photobleaching and that GFP-PatJ5-6 did not affect the FRAP kinetics of mCherry-Homer3 (Fig 7B). We then examined full-length PatJ (PatJ1-8) and the corresponding HBM. As expected, wild-type PatJ was efficiently recruited into mCherry-Homer3 condensates, whereas PatJ HBM displayed a more diffuse cytoplasmic distribution (Fig 7C). Quantification revealed a significant reduction in colocalization for the PatJ HBM compared to wild-type PatJ (Fig 7D). Intriguingly, overexpression of PatJ in 293T cells significantly reduced both TEAD and TOPFlash reporter activity and mutation of the Homer binding site partially (in case of the TEAD reporter) or completely (in case of the TOPFlash reporter) reversed this effect (Fig 7D and 7E). This suggests that PatJ acts – in part – via Homers to regulate YAP and WNT signaling. To confirm a role for PatJ in the control of

YAP/Wnt signaling, we turned to PatJ MDCK KO cells. TEAD and Wnt reporter activities were significantly reduced in MDCK cells lacking PatJ (Fig 7G and 7H), phenocopying the signaling defect observed in Homer TKO cells. Curiously, however, the transcription of canonical YAP target genes was increased whilst HAS2 and FZD4 expression was reduced in PatJ KO cells (Fig 7I and 7J). Taken together the data indicate that PatJ controls YAP and Wnt signaling upstream of Homers in a cell-type dependent and possibly non-canonical fashion.

**Homers control YAP and Wnt signaling and cell migration in colorectal cancer cells**

Homers have been implicated in Wnt/β-catenin signaling in cancer and non-cancer cells, including Wnt-driven colorectal cancer (CRC) cells [78, 79, 80, 81]. To explore the functions of Homers in YAP and Wnt signaling in CRCs, we first screened a panel of CRC cell lines for Homer expression. Homer1 and Homer3 were expressed in HCT116, DLD1 and RKO cells, whilst Homer2 was only detected in DLD1 cells (Fig 8A). Given their widespread use as a CRC model, we decided to study the functions of Homers in HCT116 cells, which express oncogenic KRAS and possess a 3bp deletion in the *CTNNB1* gene that stabilizes β-catenin, resulting in hyperactivation of Wnt signaling [82]. As expected, immunofluorescence microscopy using Homer antibodies showed that endogenous Homer1 and Homer3 formed cytoplasmic puncta in fixed HCT116 cells (Fig 8B). siRNA-mediated silencing of Homers did not notably alter the pYAP/YAP ratio or total β-catenin protein levels (Fig 8C and 8D) but significantly reduced both YAP/TEAD and TOPFlash luciferase reporter activity (Fig 8E). In addition, the expression of the YAP/TEAD target genes CTGF and PTPN14 (note that ANKRD1 was not detected in HCT116 cells by qPCR) (Fig 8F) as well as the canonical Wnt target genes HAS2, SOX9, and Axin2 (Fig 8G) was significantly reduced in Homer siRNA-transfected cells. To test if Homers promote CRC cell proliferation or migration, we silenced Homer expression using siRNAs and performed calorimetric proliferation (MTT) and scratch wound assays. Cell proliferation was unaffected upon Homer knockdown (Fig 8H). However, and remarkably, Homer siRNA-transfected cells were drastically impaired in wound closure compared to control transfected cells (Fig 8I). We concluded that Homers promote CRC cell migration by enhancing YAP/TEAD and canonical Wnt signaling.

## Discussion

Biomolecular condensates have emerged as key regulators of cell signaling including the Hippo/YAP and Wnt signaling pathways [83, 84, 85]. Here we show that Homer proteins act as scaffolds for biomolecular condensates to promote YAP/TEAD and canonical Wnt/β-catenin signaling downstream of the epithelial Crumbs complex. Our data reveal an unexpected function for the Homer protein family in YAP-Wnt signaling crosstalk and suggest that the role of the Crumbs complex in the control of Hippo/YAP signaling is much more complex than current models imply.

**Homers regulate YAP and Wnt signaling via biomolecular condensates**

It has been shown using *in vitro* reconstitutions that Homer3 phase separates with post-synaptic scaffolding proteins [86, 87, 88]. Such condensates promote actin bundling, suggesting they might act as hubs to regulate post-synaptic actin dynamics and signaling. We show here that all Homers form cytoplasmic condensates in epithelial cells and that these structures efficiently sequester PatJ, FRYL, NDR1, YAP and β-catenin (Fig 9A). Since Homers assemble into large homo- and hetero-oligomers via their C-terminal coiled-coil domains [36, 37] and coiled-coil domains are sufficient to drive phase separation [89, 90], we propose that Homer oligomerization is the major driving force for condensate assembly (Fig 9B). The fundamental

building block of such condensates are Homer tetramers [36, 37], which can interact with four PxxF motif containing ligands. If the ligand possesses more than one PxxF motif or itself assembles into oligomers, then Homer tetramers can be crosslinked into large polymeric networks that are prone to phase separate. This model is consistent with data showing that a truncated isoform of Homer1 (Homer1a) lacking the coiled-coil domain disrupts post-synaptic density condensates *in vitro* [86, 87, 88]. We show that both PatJ and FRYL are recruited into Homer condensates through EVH1 domain/PxxF motif interactions. Whilst PatJ diffused rapidly and efficiently within the condensate (~60% mobile fraction), FRYL was extraordinarily immobile (~10% mobile fraction). In addition, FRYL but not PatJ increased the mobile fraction of Homers. Based on this and our biochemical data showing that PatJ promotes the oligomerization of Homers, we propose that PatJ acts as a multivalent EVH1 domain ligand that crosslinks Homer tetramers into large hetero-oligomers and thereby solidifies Homer condensates. Conversely, FRYL may act as a "valence capping" protein that binds to Homer EVH1 domains in a monovalent manner and thereby severs connections in the Homer tetramer network, rendering Homer condensates more fluid (Fig 9B). Interestingly, although all Homers possess an identical domain architecture, condensates formed by Homer1, 2, and 3 differed markedly in shape and ultrastructure and exhibited different FRAP kinetics. The multi-lobal organisation of Homer2 condensates is particularly intriguing, as it suggests that these condensates do not efficiently exchange material upon "fusion". Such multi-phase condensates have been described before and segregate components through "demixing" [88], suggesting that Homer2 may facilitate this process. Additionally, while all Homer proteins similarly activated YAP/TEAD signaling in 293T cells, Homer3 showed a dominant effect in MDCK cells. This suggests cell type-dependent differences in how Homers are utilized. The reason for this structural and functional diversity is currently unknown, but it is tempting to speculate that individual Homers possess slightly different ligand binding or oligomerization properties [91], which could fine-tune or even alter the signaling output of Homer condensates.

We show that Homers sequester YAP and β-catenin in biomolecular condensates to promote YAP/TEAD and canonical Wnt signaling. How YAP and β-catenin become concentrated in Homer condensates is currently unclear. Previous studies have demonstrated that YAP and TAZ phase separate in the nucleus to drive TEAD-dependent transcription [92, 93, 94]. While TAZ phase separates spontaneously via its intrinsically disordered region and coiled-coil domain, YAP phase separation appears to be more regulated and may depend on cellular stimuli or partner proteins [95]. Indeed, the canonical Hippo kinases MST and LATS as well as AMOT and KIBRA, which promote the phosphorylation of YAP via LATS kinases [39, 96, 97], all phase separate with YAP in the cytoplasm to suppress YAP signaling [74, 75]. Interestingly, such "Hippo-activating" condensates can fuse or coalesce with "Hippo-inactivating" condensates containing the STRIPAK complex (a negative regulator of Hippo signaling). The fusion of such antagonistic condensates creates mixed triscaffold condensates in which the STRIPAK complex is inactivated, ultimately promoting the phosphorylation and inactivation of YAP [74]. Our data indicate that Homers drive the formation of a unique type of condensate to sequester and activate YAP. Whether the STRIPAK complex or canonical Hippo pathway regulators, such as AMOT and KIBRA are also recruited into or excluded from Homer condensates is currently unclear. A comprehensive proteomic characterization of Homer condensates is needed to answer this question and to fully elucidate the mechanism by which Homers promote YAP/TEAD signaling.

We demonstrate that PatJ and FRYL suppress YAP/TEAD signaling in 293T cells, yet with opposing dependencies on Homer binding. Whilst FRYL was significantly more potent in suppressing YAP/TEAD activity when its Homer binding site was mutated, mutation of the Homer binding site in PatJ partially reverted PatJ's inhibitory effect on YAP/TEAD signaling. This suggests that Homers interfere with the activity of the FRYL/NDR complex to limit YAP

phosphorylation, permitting YAP to drive TEAD-dependent transcription. This aligns with previous studies showing that NDR phosphorylates and inhibits YAP in the mouse intestinal epithelium and in cultured cells [4, 5]. By contrast, PatJ appears to counteract the function of Homers, reducing YAP/TEAD signaling output. This suggests a hierarchy of direct inhibitory interactions in which PatJ (or the Crumbs complex) suppresses Homers, which in turn suppress the FRYL/NDR complex (Fig 9A). Indeed, we show that inactivation of *PatJ* in MDCK cells increased YAP target gene transcription. However, and unexpectedly, TEAD (and Wnt) reporter activity was markedly reduced in *PatJ* MDCK KO cells. This suggests that PatJ can control the transcription of YAP targets via TEAD-dependent and TEAD-independent mechanisms, possibly by linking YAP to the AP-1 and SMAD2/3 transcription factors [31, 98, 99, 100]. Alternatively, the atypical signaling phenotype observed in PatJ KO MDCK cells might be caused by the mislocalisation or deregulation of direct PatJ binding partners, such as AMOT and KIBRA [39, 41, 101], or the Homer proteins. Regardless of the exact mechanism, our data clearly indicate that Homers link the Crumbs complex to a non-canonical FRYL/NDR axis to control the activity of YAP and to regulate YAP-Wnt signaling crosstalk. This signaling cascade might have important implications in polarized epithelial cells, in which the Crumbs complex links cell density sensing to the inhibition of YAP [31]. Interestingly, PatJ has recently been shown to promote the condensation of ZO-1 along the apical-lateral interface to establish a functional tight junction belt [42, 102]. It is tempting to speculate therefore that in polarized epithelia Homers phase separate with PatJ at the membrane to control YAP/TEAD and Wnt signaling from the apical lateral border.

**Role of Homers in YAP-Wnt crosstalk in colorectal cancer cells**

Most CRCs are driven by a hyperactivated Wnt/β-catenin signaling pathway. There is evidence that Wnt signaling activates YAP transcription and that YAP, in turn, promotes CRC progression [13, 14, 16, 103]. However, other studies indicate that YAP acts as a tumor suppressor in CRC [104], suggesting that the role of YAP in CRCs is context-dependent [105]. We demonstrate that Homers promote YAP/TEAD and canonical Wnt signaling in MDCK-II, 293T, and HCT116 CRC cells. This indicates a universal function of Homers in YAP and Wnt signaling and suggests a tumor promoting role in cancers that are driven by a hyperactive Wnt pathway. Interestingly, whilst Homers and FRYL acted antagonistically to regulate the expression of canonical YAP target genes, they both promoted the transcription of several genes with reported or potential functions in Wnt signaling and CRC progression: FZD4 (Frizzled-4, a Wnt receptor and potential Wnt target gene) [106, 107], GNA14 (a G-protein implicated in CRC progression) [62], DACH1 (Dachshund homolog 1, which can act as an inhibitor or activator of Wnt/β-catenin signaling) [59, 60] and HAS2 (Hyaluronic acid synthase 2, a well-documented Wnt target gene and a potential tumor promotor in CRCs) [51, 52, 53, 54, 108]. This clearly supports a role for Homers in the transcriptional control of pro-oncogenic genes. Despite this common gene signature, TOPFlash reporter and Axin2 qPCR data suggest that Homers and FRYL control the activity of the Wnt pathway via distinct TCF/LEF-dependent (Homers) and TCF/LEF-independent (FRYL) mechanisms. We therefore hypothesize that Homers and FRYL/NDR converge to control YAP but function independently to control β-catenin (Fig 9C). Indeed, there is evidence that Homer3 directly activates β-catenin via c-Src, enhancing its nuclear translocation and promoting breast cancer metastasis in mouse models [80]. Conversely, NDR has been shown to promote β-catenin degradation, suppressing metastasis in prostate cancers [109]. Although the precise mechanisms are likely more complex, the current data suggest that Homer phase separation promotes YAP and Wnt/β-catenin signaling by a) regulating the activity of the FRYL/NDR complex, b) stabilizing β-catenin or preventing its degradation via the destruction complex, c) promoting YAP activation, or d) a combination of these mechanisms (Fig 9C). In light of the close physical and functional interaction between YAP and the destruction complex

[12, 14] and recent work demonstrating that the destruction complex itself may be a phase-separated compartment [84, 110], it will be important to explore whether Homer condensates sequester or exclude components of the destruction complex and whether this has functional consequences for the coordination of YAP and Wnt signaling responses. In conclusion, we demonstrate that Homer-driven phase separation orchestrates YAP-Wnt signaling crosstalk in cancer and non-cancer cells and that the suppression of Homers may present a strategy to dampen Wnt signaling and cell motility in β-catenin-driven cancers.

**Acknowledgements**
We are grateful to Boon Chuan Low and Darren Wong Chen Pei for reagents and plasmids and Jeanette Leong and Amirul Sufyan Bin Mohamed Salleh for their contribution to this work during their Final Year Projects. This project is supported by the Ministry of Education, Singapore, under its Academic Research Fund Tier 2 (MOE-T2EP30121-0019) and Tier 1 (RG31/23).

**Author contributions**
SMJMY generated and characterized Homer KO cells, performed qPCR, reporter assays, biochemical and microscopy experiments, and analysed the data; LJW generated FRYL KO cells and performed stainings on mouse kidney sections; YC generated PatJ KO cells and performed qPCR and reporter assays; BH performed the APEX2-TEM analysis of Homer condensates; AL obtained funding, conceived the project, supervised SMJMY, LJW, YC and BH, and wrote the manuscript.

**Conflict of interest**
The authors declare no conflict of interest

## Materials & Methods

### Cell lines
Madin-Darby Canine Kidney type II (MDCK-II), Human Embryonic Kidney 293T (HEK293T), three human colorectal carcinoma HCT116,DLD-1, and RKO were used in this study. MDCK-II, HEK293T and HCT116 cells were grown in DMEM, high glucose, GlutaMAX™ pyruvate (Gibco #10569010). DLD-1 and RKO cells were grown in RPMI 1640 supplemented with L-Glutamine (Gibco #11875093). All media were supplemented with 10 % foetal bovine serum and 100 U/ml penicillin-streptomycin. All cells were grown at 37 $^{O}$C and under 5% $CO_2$. Cell lines used were not authenticated and were negative to mycoplasma contamination. For some experiments MDCK cells were seeded onto polycarbonate or polyethylene 0.4 µm-pore Transwell® filter inserts at a seeding density of approximately $2.2\times10^5$ cells/cm$^2$. Cells were grown on the filter for 10-14 days to achieve full polarisation. Media was replenished every two days.

### Bacterial strains
NEB10-beta competent *E. coli* (NEB, #C3019I) were used to transform plasmids for cloning. Bacteria were cultured in LB Agar (BD, Difco #244520) and LB Broth (BD, Difco #244620) at 37°C.

### DNA constructs
Homers, PATJ, FRYL, and NDR1 cDNAs were PCR amplified from commercial vectors, utilizing primers specifically designed to enable seamless ligation into the pEGFP-C1, p3xHA-

C1, or pEGFP-APEX2-C1 backbones [34]. PatJ and NDR1 constructs were generated using Transfer PCR (TPCR), using www.rf-cloning.org/ for primer design. Details of cDNA cloning and primers are listed in Table S1. Full-length FRYL was cloned into the pEGFP-C1 backbone using Gibson Assembly HiFi DNA Assembly Cloning Kit (NEB #E5520). Site-directed mutagenesis PCR was used to introduce specific mutations into the wild-type cDNAs. For PATJ, mutations P812A and F815A were introduced to inactivate the PxxF motif in the linker region between PDZ domains 5 and 6. Homer1 was mutated at position G89A, rendering the EVH1 domain inactive. The two PxxF motifs in FRYL were mutated to produce the mutants M1 (P2663A & P2757A) and M2 (P2663A & F2666A / P2757A & F2760A). The specific cDNAs and primers used for these mutagenesis reactions are detailed in Table S1. CRISPOR (http://crispor.org) was used to design gRNA. Three gRNAs targeting early exons were selected for each gene of interest. The gRNAs were synthesized as pairs of short oligonucleotides with 5' phosphorylated ends. These oligonucleotide pairs were annealed in annealing buffer (1 mM Tris pH 8, 5 mM NaCl, 0.5 mM EDTA in Milli-Q water) by heating the mixture to 95°C, followed by a gradual cooling to 30°C for 1 hour. The annealed gRNAs were then ligated into pSpCas9(BB)-2A-Puro (PX459) (Addgene #62988) vector digested with *BbsI*-HF® (NEB). All gRNAs used in this study are listed in Key Resource Table. All plasmids were transformed into NEB10β (NEB #C3019I) competent *E.coli*. All plasmids were screened by restriction enzyme digest or PCR and verified by DNA sequencing.

**Plasmid and gRNA transfection**

MDCK and HEK293T cells were transfected with plasmids encoding GFP- or HA-tagged proteins, and/or guide RNAs (gRNAs), when cells reached approximately 60% confluency. Prior to transfection, the culture medium was replaced with fresh antibiotic-free DMEM containing 10% FBS. Transfections were carried out using either polyethylenimine (PEI) or Lipofectamine™ 3000 (Invitrogen #L3000015), depending on the cell type. For MDCK cells, Lipofectamine 3000 was used at a ratio of 3 µL per 1 µg of plasmid DNA. For HEK293T cells, PEI was used at a ratio of 5 µL per 1 µg of plasmid DNA. In 6-well plates, a total of 2 µg DNA was used per well. For transfection in 12-well or 24-well plates, 1 µg DNA per well was used for MDCK cells. DNA and transfection reagents were diluted in DMEM or OptiMEM and incubated at room temperature for 30 minutes to allow complex formation. The transfection mix was then added dropwise to the cells. After 4 hours, the medium was replaced with complete growth medium supplemented with 10% FBS and 1% penicillin–streptomycin. Cells were allowed to grow for 16-24 hours post-transfection before being processed for downstream RNA or protein analyses.

**Generation of MDCK knockout cells**

Stable MDCK cell lines expressing EGFP-APEX2 tagged Homers [34] and PatJ knockout MDCK cells [45] have been described previously. To generate Homer and FRYL knockout cells, MDCK cells were co-transfected with 0.5 µg of PX459 plasmid (encoding Cas9 and the single-guide RNA targeting the gene of interest) and 0.1 µg of pEGFP-C1. The pEGFP-C1 plasmid encoded a neomycin (G418/geneticin) resistance cassette, allowing for antibiotic selection. 24 hours after transfection, cells were placed under 200 µg/mL G418 selection for 14 days. Surviving cells were then sorted by FACS based on GFP expression and plated as single-cell clones in 96-well plates. Clonal populations were expanded and screened for knockout efficiency by Western blotting to confirm the absence of the target protein. Knockout clones were further validated by Sanger sequencing of the targeted locus and by immunofluorescence staining to confirm the loss of protein expression at the cellular level.

**Genomic DNA Extraction and Sanger Sequencing**

Genomic DNA (gDNA) was isolated from cultured cells using the GeneJET Genomic DNA Purification Kit (Thermo Scientific #K0721) according to the manufacturer's instructions. Briefly, cells were harvested and washed twice with PBS. The resulting cell pellet was lysed in a buffer containing proteinase K to degrade cellular proteins, followed by RNase A treatment to eliminate RNA contamination. After complete lysis, ethanol was added to facilitate DNA binding to the silica membrane within the spin column. The lysate was then transferred to the spin column and centrifuged, allowing gDNA to bind to the membrane while contaminants were removed via a series of washes with the supplied buffers. The purified DNA was eluted in RNase-free water. For genotyping of CRISPR-edited loci, PCR amplification was performed using primers flanking the guide RNA target site. Primer sequences were designed using the CRISPOR online tool (http://crispor.tefor.net) to ensure specificity. PCR products were purified and submitted for Sanger sequencing (BioBasic, Singapore). Resulting chromatograms were analyzed to confirm sequence edits and to assess the efficiency of gene knockout.

**siRNA transfection**

For siRNA transfection, cells were seeded to reach approximately 50% confluency on the day of transfection. Culture medium was replaced with antibiotic-free DMEM containing 10% FBS. siRNA duplexes were transfected at a final concentration of 100 nM using Lipofectamine RNAiMAX (Invitrogen, #13778075). For every 100 nM of siRNA, 3 µL of RNAiMAX was used per well. siRNA and RNAiMAX were diluted in DMEM only media, incubated for 20–30 minutes at room temperature, and then added dropwise to cells. After 24 hours, the medium was replaced with fresh complete DMEM containing FBS and antibiotics. Cells were harvested for RNA or protein extraction 48 hours post-transfection.

**Immunoprecipitation**

MDCK or HEK293T cells transiently transfected with GFP-tagged constructs were washed twice with cold phosphate-buffered saline (PBS) and lysed in ice-cold lysis buffer composed of 50 mM Tris-HCl (pH 7.4), 150 mM NaCl, 0.5% Triton X-100, and 1 mM EDTA, supplemented with protease inhibitors (Roche cOmplete™ Mini EDTA-free, #11873580001), and, where indicated, phosphatase inhibitors (PhosSTOP™, Roche). Lysis was performed by incubating the cells with buffer for 10 minutes at 4 °C on a rotating platform. Lysates were clarified by centrifugation at 20,000 × g for 30 minutes at 4 °C. Cleared lysates were incubated with GFP-Trap® Agarose beads (Chromotek, gta-20) at a 1:20 bead-to-lysate dilution in lysis buffer. The bead–lysate mixture was incubated at 4 °C for 2 hours on a rotator to allow binding of GFP-tagged proteins. Following incubation, beads were pelleted by centrifugation at 500 × g for 2 minutes at 4 °C and washed three times with lysis buffer to remove unbound proteins. After the final wash, beads were resuspended in 4× LDS sample buffer (Invitrogen) containing 200 mM dithiothreitol (DTT). Samples were boiled at 96 °C for 5 minutes to elute bound proteins from the beads.

**SDS-PAGE and Western Blotting**

Protein lysates were mixed with 4× lithium dodecyl sulfate (LDS) sample buffer containing 200 mM dithiothreitol (DTT) and denatured by boiling at 96 °C for 5 minutes. Total protein concentrations were determined using the Bradford assay (Bio-Rad) to ensure equal loading across samples. Equal amounts of protein were separated by SDS-PAGE at 120 V for 1 hour in standard SDS running buffer (25 mM Tris base, 192 mM glycine, 0.2% SDS). Proteins were transferred onto methanol-activated polyvinylidene difluoride (PVDF) membranes (Millipore) in transfer buffer (25 mM Tris, 192 mM glycine, 20% (v/v) methanol) using a wet-transfer system, either overnight at 20 V or for 3 hours at 70 V, both at 4 °C. After transfer, membranes

were briefly dehydrated in methanol for 10 seconds and air-dried for 30 minutes to enhance protein retention. Membranes were then blocked and incubated with primary antibodies diluted in blocking buffer containing 2.5% BSA, 0.4% Tween-20, and 1 mM sodium azide. Following three washes with PBS containing 0.1% Tween-20 (PBST), membranes were incubated with species-appropriate horseradish peroxidase (HRP)-conjugated secondary antibodies diluted in 5% non-fat dry milk in PBST. After a further three washes in PBST, blots were developed using an enhanced chemiluminescent (ECL) substrate and imaged using a ChemiDoc imaging system (Bio-Rad).

**Immunofluorescence**

HEK293T cells were seeded onto fibronectin-coated glass coverslips to promote robust adhesion. MDCK cells were cultured either on glass coverslips or on Transwell® filters, depending on the experimental setup. Cells were washed three times with PBS++ (PBS supplemented with $Ca^{2+}$ and $Mg^{2+}$) and fixed with either 1% or 4% paraformaldehyde (PFA), depending on primary antibody used, in PBS++ for 10-20 minutes at room temperature, followed by three additional washes with PBS++. Cells were then permeabilised with 0.5% Triton X-100 in PBS for 10-15 minutes, washed three times in PBS, and subsequently blocked in 10% FBS in PBS for 1 hour at room temperature. For Transwell-grown monolayers, the membrane filters were carefully excised using sterile razor blades and handled with the cell-facing side up throughout all staining steps. All incubation steps, including washes, were performed in a humidified chamber to prevent drying.

Samples were incubated with primary antibodies diluted in antibody incubation buffer (0.2 µm-filtered PBS containing 0.1% BSA and 0.01% Tween-20) for 1–3 hours at room temperature. After three PBS washes, samples were incubated with fluorophore-conjugated secondary antibodies diluted in the same buffer for 1 hour at room temperature, protected from light. Following secondary antibody incubation, samples were stained with 20 ng/mL DAPI in PBS to label nuclei and washed thoroughly. Glass coverslip samples were mounted onto microscope slides using fluorescent mounting medium (Vectashield, Vector Laboratories H-1000). For Transwell® samples, the membranes were placed cell side up, overlaid with mounting medium, and covered with #1.5 (12 mm) glass coverslips (VWR). Coverslips were sealed using transparent nail polish to prevent drying and preserve fluorescence.

**Confocal Microscopy**

Fixed samples and live-cell imaging were imaged using a CorrSight spinning disk confocal microscope (Thermo Scientific) equipped with an Orca R2 CCD camera (Hamamatsu). Imaging was performed using 40x (EC Plan-Neofluar 40x/NA 1.3, Oil M27; Zeiss) or 63x (Plan-Apochromat 63x/NA 1.4, Oil M27; Zeiss) oil immersion objectives and utilizing 405, 488, 561 nm, and 633 nm lasers for excitation. Live-cell imaging was done at 5% $CO_2$ supply and 37°C. Imaging of biomolecular condensates was performed on a Zeiss LSM980 confocal microscope equipped with 63x oil immersion objectives and Airyscan detection. The images were scanned 940 × 940 pixels, unidirectionally with SR-8Y mode. Detection gain was within the range of 650 to 850. Confocal images were gain-corrected and analysed using Fiji (ImageJ) [111].

**Live-cell imaging of condensate formation**

HEK293T cells were transfected with GFP-tagged Homer1, Homer2, or Homer3 using PEI as transfection reagent. After 6 hours post-transfection, the medium was replaced with phenol red–free DMEM supplemented with 10% FBS. Images were captured at 3 min intervals for approximately 5 hours using a CorrSight spinning disk confocal microscope (ThermoScientific) equipped with an Orca R2 CCD camera (Hamamatsu) and an

environmental control chamber maintaining cells at 37°C and 5% $CO_2$ during imaging. Fluorescence excitation was achieved using a 488 nm laser for GFP, using minimal laser power and exposure times to prevent photobleaching and phototoxicity. Z-stacks using a 1 µm step size were acquired to visualise condensates throughout the cell volume. Time-lapse data was analysed using Fiji (ImageJ) [111].

**Fluorescence Recovery After Photobleaching**

HEK293T Cells were seeded onto Fibronectin-coated µ-Slide 8-Well Glass Bottom (Ibidi # 80827-90) at a density of 1x10^5 cells per well and transfected with mCherry and/or GFP plasmid with a total concentration of 0.26 µg of DNA with 1.3 µL of PEI as transfection reagent. FRAP Experiments were conducted 24-hours post-transfection in phenol red–free DMEM supplemented with 10% FBS. Live-cell imaging and FRAP were carried out using a 40x oil objective on Zeiss LSM 980 controlled by ZEN blue. Fluorescence excitation was achieved using 587 nm for mCherry or 488 nm for GFP laser. A circular region of interest (ROI) with a diameter of 1.5 µm was selected within a fluorescent condensate. Pre-bleach images were acquired at 0.5s intervals for 2s prior to photobleaching. Photobleaching was performed using 100% laser power for 2.45s to bleach the fluorescence within the ROI. Post-bleach recovery was monitored by acquiring images at 0.5s intervals for up to 50s, using minimal laser intensity to reduce phototoxicity and further bleaching. Fluorescence intensities were quantified using ZEN Blue by measuring the mean gray value within the bleached ROI and a reference ROI outside the bleached area to correct for overall photobleaching. Intensities were normalized to pre-bleach value and plotted as a function of time. Data were obtained from at least ten condensates per condition and plotted as mean ± SEM. Statistical analysis was performed using two-way ANOVA in GraphPad Prism.

**Image analysis**

For **linescan analysis** across cell junctions and condensates, a straight line was drawn across regions of interest using the "Straight Line" tool in Fiji (ImageJ). Fluorescence intensity along the line was measured using the "Analyze → Plot Profile" function, generating a plot of pixel intensity values across the selected region. For condensate linescans, raw intensity values were normalized to the maximum intensity within each profile to obtain relative fluorescence intensity. Line graphs were generated to compare fluorescence distribution between the two fluorescence channels, representing the spatial localization of each protein across the selected structure.

To quantify the **nuclear-to-cytoplasmic** distribution of YAP, fluorescence intensity measurements were performed using ImageJ. DAPI staining was used to define nuclear regions by generating nuclear masks. The mean fluorescence intensity of the YAP signal within each nucleus was measured. The cytoplasmic intensity was calculated by subtracting the nuclear signal from the total YAP signal. The nuclear-to-cytoplasmic (n/c) ratio was obtained by dividing the nuclear intensity by the cytoplasmic intensity.

**Particle analysis** was performed using Fiji (ImageJ) to quantify changes in condensate size before and after sorbitol treatment. Images of cells stained for endogenous Homer3 were adjusted using the "Threshold" function to accurately distinguish condensates from background signal, and the selected threshold range was kept constant throughout the analysis for all conditions. Binary masks were generated, and the "Analyze Particles" function was used to measure the area of individual condensates. Size filtration was set at 0.1-10 µm, to ensure inclusion of all detectable condensates.

Co-localization between two proteins within condensates was quantified using **Pearson's correlation coefficient (R)** with the Coloc2 plugin in Fiji (ImageJ). Cells were manually outlined using the Freehand Selection tool in one fluorescence channel to define the

region of interest (ROI). The same ROI was then applied to the corresponding area in the second channel to ensure spatial consistency.

**Scratch areas** for wound healing assays were measured using Fiji (ImageJ). The wound region was outlined using the Freehand Selection tool, and the area was calculated using the "Measure" function under the "Analyze" menu. The remaining wound area at each time point was normalized to the initial (0-hour) scratch area to calculate the percentage of wound closure over time.

**Electron Microscopy**

EGFP-APEX2 tagged Homer1, Homer2, and Homer3 constructs were transfected into 293T cells using PEI as transfection reagent. Cells were fixed 16-20 hours post-transfection using 2.5% glutaraldehyde (EM grade) in 0.1 M cacodylate buffer, pH 7.4 for 1 hour and further processed for APEX2-TEM as previously described [34, 76]. Electron micrographs were captured on a Tecnai T12 TEM (ThermoFisher) operated at 120 kV using an Eagle CCD camera (4k x 4k).

**RNA extraction, cDNA synthesis and RT-qPCR**

RNA was extracted using PureLink™ RNA Mini Kit (Invitrogen #12183020), following the manufacturer's protocol. To ensure the complete removal of genomic DNA from RNA preparations, 1 µg of RNA was treated with DNase I. Specifically, 1 µL of 10X reaction buffer containing $MgCl_2$, 1 µL of DNase I (TURBO DNA-free™ Kit, Invitrogen #AM1907), and DEPC-treated water to a final volume of 10 µL were incubated at 37°C for 1 hour. After digestion, 1 µL of 50 mM EDTA was added at 65°C for 10 minutes. A total of 1 µL of oligo d(T)15 primer (500 µg/mL; Integrated DNA Technologies), 1 µL of random hexamers (Integrated DNA Technologies), and 1 µL of 10 mM dNTPs. This mixture was incubated at 65°C for 5 minutes, then quickly chilled on ice at 4°C for 10 minutes to allow the primers to anneal. Following annealing, 1 µL of RiboLock RNase inhibitor, 4 µL of 5X SSIV buffer, 1 µL of 100 mM DTT, and 1 µL of reverse transcriptase enzyme (SuperScript IV Reverse Transcriptase, Invitrogen™ #18090010) were added to the annealed oligo mix. The mixture was then incubated at 23°C for 10 minutes, followed by incubation at 53°C for 10 minutes to facilitate the reverse transcription reaction. Finally, the reaction was incubated at 80°C for 10 minutes to inactivate the reverse transcriptase, and the reaction was held at 4°C until further processing. A concentration of 5 ng of cDNA were used for qPCR experiment using SsoAdvanced Universal SYBR green supermix. All qPCR primers are listed in Table S1. Each qPCR reaction was prepared in a total volume of 10 µL, containing 5 µL of SYBR Green Supermix, a mix of 0.5 µL of forward and reverse primer (10 µM), 1 µL of cDNA template (5 ng), and 3.5 µL of nuclease-free water. qPCRs were performed in 96-well plates using a Bio-Rad CFX96 thermocycler. To determine relative fold changes in gene expression, ΔΔCt values were normalised to GAPDH and control conditions (MDCK wild-type cells or control siRNA-transfected cells).

**RNA sequencing**

RNA sequencing (RNA-seq) of Homer triple knockout (TKO) MDCK cells was performed by NovogeneAIT using an Illumina sequencing platform. Total RNA was extracted and subjected to poly-A selection prior to library preparation. A non-stranded library preparation method was employed, and sequencing was conducted using paired-end reads with a read length of 150 base pairs for each end (2 × 150 bp), resulting in a total of 300 base pairs per fragment. Approximately 80 million reads were generated per sample, consisting of 40 million reads for read 1 and 40 million reads for read 2. NovogeneAIT provided raw sequencing data along with a comprehensive report including quality control (QC) metrics, alignment statistics, and

preliminary differential expression results. Downstream analysis of RNA-seq data, including differential gene expression, was performed using R.

**Heatmaps of RNA-seq** data were generated using RStudio to visualize gene expression patterns across different experimental conditions. Raw gene expression data were normalized to eliminate technical variability and log-transformed to stabilize variance across samples. The processed data were structured as a matrix with genes as rows and samples as columns. Heatmaps were generated using the pheatmap package in R, selected for its flexibility and user-friendly interface. The pheatmap function was used to create the heatmaps, with both rows (genes) and columns (samples) hierarchically clustered based on expression similarity using default distance and linkage settings.

The top 100 upregulated and downregulated genes identified from the RNA sequencing data were further analyzed for Gene Ontology (GO) enrichment using the ShinyGO 0.8 platform (http://bioinformatics.sdstate.edu/go/). This analysis allowed for the identification of significantly enriched biological processes, molecular functions, and cellular components associated with the differentially expressed genes. Gene functions were subsequently classified into specific functional groups using the **PANTHER classification system** (https://www.pantherdb.org/), facilitating a more detailed understanding of the roles these genes play in various biological pathways.

Volcano plots were generated in R to visualize differentially expressed genes based on $\log_2$ fold change and adjusted p-values from RNA-seq analysis. Processed differential expression results, including $\log_2$ fold change and adjusted p-values (padj), were imported into R as a data frame. Genes were classified as significantly up- or downregulated based on defined thresholds (e.g., $|\log_2 FC| \geq 1$ and $padj < 0.05$). The EnhancedVolcano package was used to create the plot. The EnhancedVolcano() function was applied, with $\log_2$ fold change on the x-axis and $-\log_{10}(padj)$ on the y-axis. Custom colour coding and labelling were used to highlight significantly regulated genes.

**Luciferase reporter assays**

TEAD (8xGTIIC) and TOPFlash luciferase reporter assays were performed using the Dual-Glo® Luciferase Assay System (Promega, #E2920) to measure the transcriptional activity of TEAD and TCF/LEF, respectively. For 24-well format experiments, cells were transfected with either 0.4 µg of 8xGTIIC firefly luciferase plasmid (Addgene, #34615) or 0.4 µg of TOPFlash firefly luciferase plasmid (Addgene, #12456), along with 0.04 µg of pRL-TK Renilla luciferase control reporter vector (Promega, #E2241), which served as an internal control for transfection efficiency. After 24–48 hours post-transfection, 100 µL of Dual-Glo® Luciferase Reagent (containing lysis buffer and substrate) was added directly to the wells containing 100 µL of culture medium. The plate was gently mixed and incubated at room temperature for 10 minutes to allow development of the firefly luciferase signal. The mixture was then transferred to a 96-well white opaque plate (Thermo Fisher, #15042), and luminescence was measured using a plate reader. Firefly luciferase activity, representing TEAD or TCF/LEF transcriptional activity, was detected at 560 nm emission. Next, 100 µL of Dual-Glo® Stop & Glo® Reagent was added to each well to simultaneously quench the firefly signal and activate Renilla luciferase. Renilla luminescence, which serves as a normalization control, was measured immediately afterward, at 480 nm. Firefly luciferase values were normalized to corresponding Renilla luciferase values to account for variability in transfection efficiency. Final results were expressed as the ratio of firefly to Renilla luminescence and further normalized to wild-type or control siRNA conditions to provide a relative measure of transcriptional activity.

**Quantifications and Statistical Analysis**

All statistical analyses were conducted using two-tailed paired Student's t-test analysis in GraphPad Prism, except for qPCR analysis, which was performed using a Two-way ANOVA with Tukey's multiple comparison tests. FRAP statistical analysis was performed using Two-way ANOVA. Significance of data is represented as ns, not significant, * $P \leq 0.05$, ** $P \leq 0.01$, *** $P \leq 0.001$, **** $P \leq 0.0001$. Error bars in all figures represent mean +/- SEM.

**Figure legends:**

**Figure 1: Homers localise to apical cell junctions in renal epithelial cells**
(A) Localisation of Homers in MDCK-II cells. Cells were grown to confluency on Transwell filters, fixed and stained with Homer1, Homer2 or Homer3 antibodies. Both XY (en face) and XZ (side view) projections of confocal z-stacks are shown. Note that anti-Homer1 antibodies produce a non-specific staining of unknown identity in the cytoplasm (yellow asterisks). (B-D) Localisation of Homer1 in mouse kidney cryosections. Sections were stained with antibodies against Homer1 and ZO-1 and counterstained with phalloidin and DAPI. (B) Cross-section through renal tubules. (C) Magnified views of apical cell junctions based on the images shown in (B). (D) En face sections through apical cell junctions in renal epithelial cells.

**Figure 2: Homers are recruited to apical cell junctions via a direct interaction with PatJ**
(A) PATJ contains two evolutionarily conserved PxxF motifs; one in the PDZ4 domain, the other in the linker region between PDZ domains 5 and 6. Mm: *Mus musculus*, Rn: *Rattus norvegicus*, Cf: *Canis lupus familiaris*, Hs: *Homo sapiens* (B) Schematic representation of PATJ truncation and PxxF mutant constructs cloned into the APEX2-EGFP-C1 (A2E-C1) expression vector. (C) Co-immunoprecipitation (Co-IP) assay in 293T cells transfected with the indicated constructs. GFP-tagged proteins were pulled down using GFP-Trap beads and interaction with endogenous Homer proteins was assessed by Western blotting (WB). (D) Co-IP assay of A2E-GFP-PATJ1-8 and the corresponding PxxF mutant. (E) Co-IP assay of GFP-PatJ5-6 with HA-tagged wild-type Homer1 or the HA-tagged Homer1 EVH1 domain mutant (G89A). (F) Co-IP assay of GFP-PatJ5-6 with HA-tagged wild-type Homer1 or the HA-tagged Homer1 EVH1 domain. (G) Sucrose density gradient centrifugation of 293T cell lysates. Cells were transfected with the A2E-C1 construct (control; top) or the A2E-GFP-PATJ1-8 construct (bottom). Gradient fractions were probed with GFP and Homer1 antibodies. (H) Maximum intensity projections of confocal z-stacks of MDCK wild-type (WT) and PATJ KO cells co-cultured on Transwell filters. Cells were stained with antibodies against Homer1, Homer2, and Homer3 (top panels). PALS1 staining (bottom panel) served as a marker for WT cells. (I) Average junctional signal intensity of Pals1 and Homers in PATJ KO and MDCK WT cells determined by line scan analysis (n=11 each). (J) WB analysis of MDCK WT and PATJ KO MDCK cell lysates probed for PALS1, PATJ and Homers.

**Figure 3: Homers regulate YAP and WNT signalling**
(A) Volcano plot showing select differentially expressed genes (DEGs) in Homer TKO cells identified by RNA-sequencing. (B) KEGG pathway analysis of DEGs in Homer TKO cells. The y-axis lists significantly enriched pathways, while the x-axis represents the gene ratio. Dot size indicates the number of DEGs involved in each pathway, and colour reflects the adjusted p-value (padj), with red indicating higher statistical significance. (C) Bar graphs showing the log2 fold changes of DEGs associated with the YAP (top) and WNT (bottom) signalling pathways. Genes were selected based on their relevance to each pathway. (D) WB analysis of WT MDCK and Homer TKO cell lysates probed for YAP and pYAP (S127). The pYAP/YAP ratio was quantified by densitometry (n=3). (E) TEAD luciferase activity in Homer TKO cells

normalised to MDCK WT cells (n=4). (F and G) qPCR analysis of canonical YAP target genes (F) and WNT-associated genes (G) in Homer TKO cells (n=4). (H) qPCR analysis of Axin2 expression in Homer TKO cells (n=4). (I) TOPFlash luciferase activity in Homer TKO cells normalised to MDCK WT cells (n=3). (J) qPCR analysis of YAP target genes in 293T cells transfected with control siRNA or a pool of siRNAs targeting all three Homers (n=3). (K) TEAD luciferase assay of 293T cells transfected with GFP or GFP-tagged YAP, Homer1, Homer2 or Homer3 (n=3). (L) TOPFlash luciferase activity of 293T cells transfected with a total of 100 nM of control siRNA or a pool of siRNAs targeting all three Homers (n=3). (M) TOPFlash luciferase activity in 293T cells transfected with GFP or GFP-tagged Homer1, Homer2, or Homer3 (n=3). All Luciferase assays were statistically analysed using a paired Student's t-test. All qPCR data were analysed using Two-Way ANOVA Tukey multiple comparison test. Data is presented as mean ± SEM. *P ≤ 0.05; **P ≤ 0.01; ***P ≤ 0.001; ****P ≤ 0.0001.

**Figure 4: The NDR kinase scaffolding protein FRYL interacts with Homers and suppresses YAP/TEAD signaling**

(A) STRING interactome of FRYL based on evidence for physical interactions. (B) Diagram of full-length FRYL and the two Homer binding mutant (HBM) constructs M1 and M2 with distinct mutations in the two PxxF motifs. (C) Co-IP assays of 293T cells transfected with WT full-length FRYL-GFP or the two FRYL HBMs M1 and M2. Membranes were probed for GFP, FRYL and endogenous Homers. (D) WB analysis of MDCK WT and FRYL KO cell lysates probed for FRYL, YAP and p-YAP (S127). The p-YAP/YAP ratio was quantified by densitometric analysis (n=3). (E) TEAD luciferase activity in FRYL KO cells normalised to MDCK WT cells. (F) FRYL KO and MDCK WT cells were cultured on Transwell filters, fixed and stained for total YAP. Nuclear and cytoplasmic YAP signal intensities were quantified using ImageJ, using DAPI staining as a mask to define the nucleus. Quantification was performed on 10 images per condition, analyzing more than 80 cells per image (n = ~800 cells). Data is presented as mean ± SEM. **P ≤ 0.01, ****P ≤ 0.0001 (Student's t-test). (G and H) qPCR analysis of YAP target genes (G) and WNT-associated genes (H) in FRYL KO cells (n=3). (I) qPCR analysis of Axin2 mRNA levels in FRYL KO cells (n=3). (J) TOPFlash luciferase activity in FRYL KO cells normalized to MDCK WT cells (n=3). (K) Co-IP analysis of 293T cells transfected with GFP or GFP-NDR1. Membranes were probed with antibodies against NDR1, FRYL, MOB1a and LATS1. (L) WB analysis of 293T cells transfected with GFP or GFP-FRYL. Membranes were probed with the indicated antibodies. (M) TEAD luciferase activity of 293T cells co-transfected with 8xGTIIC-luciferase reporter plasmid and either GFP, WT GFP-FRYL, or GFP-FRYL HBM M2 (n=5). (N) qPCR analysis of YAP target genes in 293T cells transfected with a total of 100 nM of either control siRNA or FRYL siRNA (n=3). All Luciferase assays were statistically analysed using a paired Student's t-test. All qPCR data were analysed using Two-Way ANOVA Tukey multiple comparison test. Data is presented as mean ± SEM. *P ≤ 0.05; **P ≤ 0.01; ***P ≤ 0.001; ****P ≤ 0.0001.

**Figure 5: Homers form cytoplasmic biomolecular condensates**

(A and B) Confocal micrographs of 293T cells transfected with GFP-Homer1, GFP-Homer2 or GFP-Homer3 (A) and WT GFP-FRYL or GFP-FRYL HBM M2 (B). Maximum intensity projections (MIPs) are shown. (C) MIPs of 293T stained for endogenous Homer1, Homer2 or Homer3. (D) MIPs of 293T cells grown in iso-osmotic medium (non-treated; NT) or in medium containing 0.4 M sorbitol for 30 or 90 minutes stained for endogenous Homer3. Particle size analysis was performed in ImageJ. Puncta were identified based on intensity and size thresholds, and their total area/cell and frequency were quantified. Data is presented as mean ± SEM. ***P ≤ 0.001; ****P ≤ 0.0001 (Student's t-test). (E) 293T cells were transfected with

GFP-tagged Homer constructs and imaged live 6 hours post-transfection using spinning disk microscopy. Representative time frames illustrating the growth and maturation of Homer condensates are shown. The gain in the insets shown at 7.5 hrs was increased to show diffuse cytoplasmic localisation. (F) Live cell imaging illustrating the fusion and coalescence of condensates formed by GFP-tagged Homer1, Homer2, and Homer3. Green arrowheads indicate the prospective site of fusion, yellow arrowheads mark the post-fusion structures. (G) Transmission electron micrographs of 293T cells transfected with APEX2-EGFP tagged Homer1, Homer2 or Homer3. Boxed areas are magnified. Note the distinct ultrastructure of Homer condensates. N=nucleus. (H) Quantification of condensate size and circularity based on TEM. ****$P \leq 0.0001$ (One-Way ANOVA, n=12-16 condensates). (I) FRAP analysis of GFP-Homer1, GFP-Homer2 or GFP-Homer3 transfected into 293T cells. Data is presented as mean ± SEM. Statistical analysis was performed using two-way ANOVA. ** $P \leq 0.01$.

**Figure 6: Homers recruit FRYL, NDR1, YAP, and β-catenin into cytoplasmic condensates**
(A and B) 293T cells were co-transfected with HA-Homer1 and either GFP-FRYL (A) or the GFP-FRYL HBM construct M2 (B). (C) 293T cells were transfected with GFP-FRYL and stained for endogenous Homer3. (D) The Pearson's correlation coefficient (R) was calculated to quantify co-localization between HA-Homer1 and GFP-FRYL or GFP-FRYL HBM M2 (left). The size of HA-Homer1–positive condensates in cells co-transfected with GFP-FRYL or GFP-FRYL HBM M2 was measured (right). (E) FRAP analysis of mCherry-Homer3 in 293T cells co-transfected with either GFP-FRYL or GFP-FRYL HBM M2. (F and G) 293T cells were co-transfected with HA-Homer2 and GFP-NDR1 (F) or HA-Homer2 and YAP-GFP (G). Examples of large (top) and small (bottom) condensates containing HA-Homer2 and Yap-GFP are shown. (H) 293T cells were co-transfected with mCherry-Homer3 and β-catenin-GFP. (I and J) FRAP analysis of 293T cells co-transfected with mCherry-Homer3 and YAP-GFP (I) or mCherry-Homer3 and β-catenin-GFP (J). All FRAP data is presented as mean ± SEM. Statistical analysis was performed using two-way ANOVA. ** $P \leq 0.01$, *** $P \leq 0.001$, **** $P \leq 0.0001$. Zoomed-in images in panels A-C and F-H show representative regions of co-localization. Relative fluorescence intensity profiles along the line were plotted and normalized to the maximum intensity value for each channel.

**Figure 7: PatJ regulates YAP and WNT signaling, in part via Homers**
(A) 293T cells co-transfected with mCherry-Homer3 and GFP-PATJ PDZ 5-6 were fixed and stained for endogenous YAP. Zoomed-in images show regions of co-localization. Relative fluorescence intensity profiles along the line were plotted and normalized to the maximum intensity value for each channel. (B) FRAP analysis of 293T cells co-transfected with mCherry-Homer3 and GFP-PATJ PDZ 5-6. FRAP analysis was performed as described in Figure 6. (C) 293T cells were co-transfected with mCherry-Homer3 and GFP-PATJ PDZ1–8 or the GFP-PATJ PDZ1-8 HBM construct. Zoomed-in images show regions of co-localization. (D) Co-localization between mCherry-Homer3 and GFP-PATJ variants was quantified using Pearson's R. Data is presented as mean ± SEM. Statistical significance was assessed using Student's t-test. (E and F) TEAD and TOPFlash luciferase reporter assays in 293T cells transfected with GFP, GFP-PATJ PDZ1-8 or the GFP-PATJ PDZ1-8 HBM construct (n=4). (G and H) TEAD and TOPFlash luciferase reporter assays in MDCK WT and PatJ KO cells (n=3). (I and J) qPCR analysis of YAP (I) and Wnt (J) target genes in MDCK WT and PatJ KO cells (n=6). Data is presented as mean ± SEM. Luciferase assay data were analysed using a paired Student's t-test. qPCR data were analysed using Two-Way ANOVA. * $P \leq 0.05$, ** $P \leq 0.01$, *** $P \leq 0.001$, **** $P \leq 0.0001$.

**Figure 8: Homers promote YAP/WNT signaling and migration in HCT116 colorectal cancer cells**
(A) WB analysis of three colorectal cancer cell lines (HCT116, DLD-1, and RKO) and two non-cancerous cell lines (MDCK-II and HEK293T), probed for the expression of YAP, phosphorylated YAP (S127), Homer1, Homer2, and Homer3. (B) MIPs of HCT116 cells stained with antibodies against Homer1 or Homer3. Yellow arrows highlight small puncta in the cytoplasm. (C) WB analysis of HCT116 cells treated with control siRNA or a pool of siRNAs targeting all three Homers. Cell lysates were collected 48 hours post-transfection and probed for Homer1, Homer3, YAP, pYAP (S127), and β-catenin. (D) Quantification of the pYAP/YAP ratio based on Western blotting in (C) (n = 3). (E) HCT116 cells were transfected with control siRNA or a pool of siRNAs targeting all three Homers (n=3). (F and G) qPCR analysis of YAP target genes (F) and WNT-associated genes (G) in siRNA-transfected HCT116 cells. (H) MTT assay of siRNA-transfected HCT116 cells. The average proliferation rate of two independent experiments is shown. (I) Wound healing assay of siRNA transfected HCT116 cells. Following siRNA transfection, cells were serum-starved for 6 hours prior to scratch induction and maintained in low-serum media. Wound areas were quantified using ImageJ and normalised to the 0-hour time point (n=3). Data is presented as mean ± SEM. Statistical analysis was performed using two-way ANOVA. * $P \leq 0.05$, ** $P \leq 0.01$, *** $P \leq 0.001$, **** $P \leq 0.0001$.

**Figure 9: Model of PatJ and FRYL function in Homer-mediated YAP-WNT signaling crosstalk**
(A) Homer condensates sequester FRYL, NDR1, YAP, β-catenin and PATJ. Homers and FRYL form the immobile fraction of the condensate (dotted circle) whilst YAP, PATJ, and β-catenin are more mobile and exchange rapidly with the cytoplasmic dilute phase. (B) Putative mechanism of how PATJ and FRYL regulate Homer tetramer crosslinking in condensates. PATJ acts as a multivalent EVH1 domain ligand and crosslinks Homer tetramers into large hetero-oligomers, rendering Homers relatively immobile. Oligomerisation of PATJ itself may be mediated by PDZ/PDZ domain interactions or via an unknown PDZ domain "crosslinker" protein. Conversely, FRYL acts as a monovalent EVH1 domain ligand and severs connections in the tetramer network, increasing the mobility of Homers. (C) Speculative mechanism of how Homers and FRYL/NDR control YAP-Wnt signaling crosstalk (see discussion). The model assumes that Homers and NDR have opposing functions in regulating β-catenin [80, 109] and that cytoplasmic YAP suppresses canonical Wnt signaling by promoting β-catenin degradation or by preventing its nuclear translocation [11, 12, 14].

**Supplemental Figure legends:**

**Figure S1: Generation and characterisation of Homer KO cells**
(A) WB analysis of single Homer1, Homer2, and Homer3 knockout (KO) MDCK cell lines. Note that a truncated version of Homer2 protein is detected in KO clone #1 (asterisk). (B) MDCK WT cells were co-cultured with single Homer1, Homer2 or Homer3 KO cells on Transwell filter and stained for the corresponding Homer protein. Dotted lines represent the boundary between the single KO cells and MDCK WT cells. Note that anti-Homer1 antibodies produce a non-specific, non-junctional staining that persists in Homer1 KO cells (yellow asterisks). Note also that Homer2 protein is detected but reduced in Homer2 KO clone #1. (C) Amino acid sequence alignment of single Homer1, Homer2, and Homer3 KO cells compared to MDCK WT at their respective loci. Red asterisks (*) indicate premature stop codons. The red line marks the point at which the sequence between KO and WT genomic DNA diverges. (D) Validation of Homer TKO cells. WB analysis of Homer TKO and MDCK WT cell lysates

probed for all three Homer proteins. (E) qPCR analysis of Homer1, Homer2 and Homer3 mRNA expression in Homer TKO cell lines (n=2). (F) Homer TKO and MDCK WT cells were co-cultured on Transwell filters for 10-14 days, fixed and stained for Homer1, Homer2 or Homer3. The dotted lines represent the boundaries between the two cell populations. Non-specific staining of Homer1 antibody is indicated with yellow asterisks. (G) Homers are not required for the assembly or maintenance of the apical junctional complex. MDCK WT and Homer TKO (GFP positive) cells were co-cultured on Transwell filters, fixed and stained for junctional markers β-catenin, ZO-1, Occludin, PatJ, and Pals1. The dotted lines delineate the boundaries between WT and Homer TKO cell populations.

**Figure S2: Homers differentially regulate YAP/TEAD activity in MDCK cells**
(A) Heatmap showing the top 100 upregulated and top 100 downregulated genes in Homer TKO MDCK cells compared to MDCK WT cells, as identified by RNA-seq analysis (n=3). Colour intensity represents relative expression levels, with red indicating upregulation and blue indicating downregulation. See Table S2 for a complete list of all differentially expressed genes along with their log2 fold changes and raw RNA-seq output. (B) The top 100 upregulated and top 100 downregulated genes were classified by PANTHER: Protein Class. Genes in the classification groups are listed in boxes. (C) TEAD luciferase activity in single Homer1, Homer2 and Homer3 KO cells normalised to MDCK WT cells (n=4). (D) qPCR analysis of YAP target gene expression in single Homer1, Homer2 and Homer3 KO cells normalised to MDCK WT cells (n=3 or 4). (E) WB analysis of MDCK WT and Homer3 KO cell lysates probed for YAP and pYAP (S127). The pYAP/YAP ratio was quantified by densitometric analysis (n=3). (F) WB analysis of MDCK WT cells and MDCK cells stably transfected with APEX2-GFP-Homer1 or APEX2-GFP-Homer3. (G) Representative confocal micrographs of MDCK cells stably transfected with APEX2-GFP-Homer1 or APEX2-GFP-Homer3 grown on Transwell filter for 10-14 days. (H) TEAD and TOPFlash luciferase assays of MDCK WT cells and MDCK cells stably transfected with APEX2-GFP-Homer1 or APEX2-GFP-Homer3 (n=5). Data is presented as mean ± SEM. Statistical significance is indicated as follows: *$P \leq 0.05$; **$P \leq 0.01$; ***$P \leq 0.001$; ****$P \leq 0.0001$.

**Figure S3: Downregulation of individual or all three Homers in HEK293T cells reduces YAP target gene transcription**
(A) WB analysis of HEK293T cells transfected with a total of 100 nM siRNA targeting either Homer1, Homer2, or Homer3, or all three Homers simultaneously. (B) qPCR analysis of HEK293T cells transfected with a total of 100 nM siRNA targeting Homer1, Homer2, or Homer3 individually or in combination. Note the significant reduction in YAP target gene transcription in all cases.

**Figure S4: LC-MS/MS of Homer3 interacting proteins**
IP-MS data of GFP-Homer3 stably overexpressed in MDCK cells. The table shows the top-ranked proteins based on peptide count identified in the MS results.

**Figure S5: Ultrastructure of Homer condensates**
(A) Representative confocal images of live HEK293T cells transfected with APEX2-EGFP tagged Homer1, Homer2, or Homer3 16-24 hrs post-transfection. (B) Representative transmission electron micrographs of HEK293T cells transfected with APEX2-EGFP tagged Homer1, Homer2, or Homer3. Arrowheads indicate Homer condensates. N=nucleus.

**Figure S6: Pearson's colocalisation and FRAP analysis**

(A) Summary of all Pearson's R values. (B) Summary of all FRAP kinetics data. Recovery refers to the measured fluorescence intensity 50 sec post-bleaching normalised to the pre-bleaching intensity (1 equals full recovery).

**Supplemental Tables:**

**Table S1: qPCR primers and oligonucleotides**
**Table S2: RNA sequencing data.** Differentially expressed genes confirmed by qPCR are highlighted.

**Supplemental Movies:**

**Movie S1:** Formation of Homer1 condensates in live cells
**Movie S2:** Formation of Homer2 condensates in live cells
**Movie S3:** Formation of Homer3 condensates in live cells
**Movie S4:** Fusion events of Homer1 condensates in live cells
**Movie S5:** Coalescence of Homer2 condensates in live cells
**Movie S6:** Coalescence of Homer3 condensates in live cells

## References


1. Ma S, Meng Z, Chen R, Guan KL. The Hippo Pathway: Biology and Pathophysiology. *Annu Rev Biochem* **88**, 577-604 (2019).

2. Misra JR, Irvine KD. The Hippo Signaling Network and Its Biological Functions. *Annual review of genetics* **52**, 65-87 (2018).

3. Thompson BJ, Sahai E. MST kinases in development and disease. *The Journal of cell biology* **210**, 871-882 (2015).

4. Zhang L*, et al.* NDR functions as a physiological YAP1 kinase in the intestinal epithelium. *Curr Biol* **25**, 296-305 (2015).

5. Irie K, Nagai T, Mizuno K. Furry protein suppresses nuclear localization of yes-associated protein (YAP) by activating NDR kinase and binding to YAP. *The Journal of biological chemistry* **295**, 3017-3028 (2020).

6. Panciera T, Azzolin L, Cordenonsi M, Piccolo S. Mechanobiology of YAP and TAZ in physiology and disease. *Nat Rev Mol Cell Biol* **18**, 758-770 (2017).

7. Manning SA, Kroeger B, Harvey KF. The regulation of Yorkie, YAP and TAZ: new insights into the Hippo pathway. *Development* **147**, (2020).

8. Rausch V, Hansen CG. The Hippo Pathway, YAP/TAZ, and the Plasma Membrane. *Trends Cell Biol* **30**, 32-48 (2020).

9. Low BC, Pan CQ, Shivashankar GV, Bershadsky A, Sudol M, Sheetz M. YAP/TAZ as mechanosensors and mechanotransducers in regulating organ size and tumor growth. *FEBS Lett* **588**, 2663-2670 (2014).

10. Meng Z, Moroishi T, Guan KL. Mechanisms of Hippo pathway regulation. *Genes Dev* **30**, 1-17 (2016).

11. Varelas X*, et al.* The Hippo pathway regulates Wnt/beta-catenin signaling. *Dev Cell* **18**, 579-591 (2010).

12. Azzolin L*, et al.* YAP/TAZ incorporation in the beta-catenin destruction complex orchestrates the Wnt response. *Cell* **158**, 157-170 (2014).

13. Rosenbluh J*, et al.* beta-Catenin-driven cancers require a YAP1 transcriptional complex for survival and tumorigenesis. *Cell* **151**, 1457-1473 (2012).

14. Imajo M, Miyatake K, Iimura A, Miyamoto A, Nishida E. A molecular mechanism that links Hippo signalling to the inhibition of Wnt/beta-catenin signalling. *The EMBO journal* **31**, 1109-1122 (2012).

15. Heallen T*, et al.* Hippo pathway inhibits Wnt signaling to restrain cardiomyocyte proliferation and heart size. *Science* **332**, 458-461 (2011).

16. Konsavage WM, Jr., Kyler SL, Rennoll SA, Jin G, Yochum GS. Wnt/beta-catenin signaling regulates Yes-associated protein (YAP) gene expression in colorectal carcinoma cells. *The Journal of biological chemistry* **287**, 11730-11739 (2012).

17. Park HW*, et al.* Alternative Wnt Signaling Activates YAP/TAZ. *Cell* **162**, 780-794 (2015).

18. Li N, Lu N, Xie C. The Hippo and Wnt signalling pathways: crosstalk during neoplastic progression in gastrointestinal tissue. *The FEBS journal* **286**, 3745-3756 (2019).

19. Zhan T, Rindtorff N, Boutros M. Wnt signaling in cancer. *Oncogene* **36**, 1461-1473 (2017).

20. Schatoff EM, Leach BI, Dow LE. Wnt Signaling and Colorectal Cancer. *Curr Colorectal Cancer Rep* **13**, 101-110 (2017).

21. Margolis B. The Crumbs3 Polarity Protein. *Cold Spring Harb Perspect Biol* **10**, (2018).

22. Tepass U. The apical polarity protein network in Drosophila epithelial cells: regulation of polarity, junctions, morphogenesis, cell growth, and survival. *Annu Rev Cell Dev Biol* **28**, 655-685 (2012).

23. Martin E, Girardello R, Dittmar G, Ludwig A. New insights into the organization and regulation of the apical polarity network in mammalian epithelial cells. *The FEBS journal*, (2021).

24. Fulford A, Tapon N, Ribeiro PS. Upstairs, downstairs: spatial regulation of Hippo signalling. *Curr Opin Cell Biol* **51**, 22-32 (2018).

25. Karaman R, Halder G. Cell Junctions in Hippo Signaling. *Cold Spring Harb Perspect Biol* **10**, (2018).

26. Chen CL*, et al.* The apical-basal cell polarity determinant Crumbs regulates Hippo signaling in Drosophila. *Proceedings of the National Academy of Sciences of the United States of America* **107**, 15810-15815 (2010).

27. Grzeschik NA, Parsons LM, Allott ML, Harvey KF, Richardson HE. Lgl, aPKC, and Crumbs regulate the Salvador/Warts/Hippo pathway through two distinct mechanisms. *Curr Biol* **20**, 573-581 (2010).

28. Ling C*, et al.* The apical transmembrane protein Crumbs functions as a tumor suppressor that regulates Hippo signaling by binding to Expanded. *Proceedings of the National Academy of Sciences of the United States of America* **107**, 10532-10537 (2010).

29. Robinson BS, Huang J, Hong Y, Moberg KH. Crumbs regulates Salvador/Warts/Hippo signaling in Drosophila via the FERM-domain protein Expanded. *Curr Biol* **20**, 582-590 (2010).

30. Szymaniak AD, Mahoney JE, Cardoso WV, Varelas X. Crumbs3-Mediated Polarity Directs Airway Epithelial Cell Fate through the Hippo Pathway Effector Yap. *Dev Cell* **34**, 283-296 (2015).

31. Varelas X*, et al.* The Crumbs complex couples cell density sensing to Hippo-dependent control of the TGF-beta-SMAD pathway. *Dev Cell* **19**, 831-844 (2010).

32. Whiteman EL*, et al.* Crumbs3 is essential for proper epithelial development and viability. *Molecular and cellular biology* **34**, 43-56 (2014).

33. Weide T*, et al.* Pals1 Haploinsufficiency Results in Proteinuria and Cyst Formation. *Journal of the American Society of Nephrology : JASN* **28**, 2093-2107 (2017).

34. Tan B, Yatim S, Peng S, Gunaratne J, Hunziker W, Ludwig A. The Mammalian Crumbs Complex Defines a Distinct Polarity Domain Apical of Epithelial Tight Junctions. *Curr Biol* **30**, 2791-2804 e2796 (2020).

35. Shiraishi-Yamaguchi Y, Furuichi T. The Homer family proteins. *Genome Biol* **8**, 206 (2007).

36. Hayashi MK, Ames HM, Hayashi Y. Tetrameric hub structure of postsynaptic scaffolding protein homer. *J Neurosci* **26**, 8492-8501 (2006).

37. Hayashi MK*, et al.* The postsynaptic density proteins Homer and Shank form a polymeric network structure. *Cell* **137**, 159-171 (2009).

38. Xiao B*, et al.* Homer regulates the association of group 1 metabotropic glutamate receptors with multivalent complexes of homer-related, synaptic proteins. *Neuron* **21**, 707-716 (1998).

39. Sugihara-Mizuno Y*, et al.* Molecular characterization of angiomotin/JEAP family proteins: interaction with MUPP1/Patj and their endogenous properties. *Genes Cells* **12**, 473-486 (2007).

40. Wells CD*, et al.* A Rich1/Amot complex regulates the Cdc42 GTPase and apical-polarity proteins in epithelial cells. *Cell* **125**, 535-548 (2006).

41. Duning K*, et al.* KIBRA modulates directional migration of podocytes. *Journal of the American Society of Nephrology : JASN* **19**, 1891-1903 (2008).

42. Pombo-Garcia K, Adame-Arana O, Martin-Lemaitre C, Julicher F, Honigmann A. Membrane prewetting by condensates promotes tight-junction belt formation. *Nature* **632**, 647-655 (2024).

43. Michel D, Arsanto JP, Massey-Harroche D, Beclin C, Wijnholds J, Le Bivic A. PATJ connects and stabilizes apical and lateral components of tight junctions in human intestinal cells. *Journal of cell science* **118**, 4049-4057 (2005).

44. Beneken J, *et al.* Structure of the Homer EVH1 domain-peptide complex reveals a new twist in polyproline recognition. *Neuron* **26**, 143-154 (2000).

45. Martin E, *et al.* Bulk exocytosis of large intracellular apical precursor organelles establishes apical domain identity during de novo lumen formation. *bioRxiv*, 2025.2003.2006.641813 (2025).

46. Wang Y, *et al.* Comprehensive Molecular Characterization of the Hippo Signaling Pathway in Cancer. *Cell reports* **25**, 1304-1317 e1305 (2018).

47. Zhou X, *et al.* YAP Aggravates Inflammatory Bowel Disease by Regulating M1/M2 Macrophage Polarization and Gut Microbial Homeostasis. *Cell reports* **27**, 1176-1189 e1175 (2019).

48. Cai J, *et al.* A RhoA-YAP-c-Myc signaling axis promotes the development of polycystic kidney disease. *Genes Dev* **32**, 781-793 (2018).

49. Venkatasubramanian G, Kelkar DA, Mandal S, Jolly MK, Kulkarni M. Analysis of Yes-Associated Protein-1 (YAP1) Target Gene Signature to Predict Progressive Breast Cancer. *J Clin Med* **11**, (2022).

50. Liu M, Zhao S, Lin Q, Wang XP. YAP regulates the expression of Hoxa1 and Hoxc13 in mouse and human oral and skin epithelial tissues. *Molecular and cellular biology* **35**, 1449-1461 (2015).

51. Xu X, Wang L, Liu B, Xie W, Chen YG. Activin/Smad2 and Wnt/beta-catenin up-regulate HAS2 and ALDH3A2 to facilitate mesendoderm differentiation of human embryonic stem cells. *The Journal of biological chemistry* **293**, 18444-18453 (2018).

52. Hurlstone AF, *et al.* The Wnt/beta-catenin pathway regulates cardiac valve formation. *Nature* **425**, 633-637 (2003).

53. Sun Y, Ying X, Li R, Weng M, Shi J, Chen Z. FGF9 Promotes Expression of HAS2 in Palatal Elevation via the Wnt/beta-Catenin/TCF7L2 Pathway. *Biomolecules* **12**, (2022).

54. Li Z, Lim SK, Liang X, Lim YP. The transcriptional coactivator WBP2 primes triple-negative breast cancer cells for responses to Wnt signaling via the JNK/Jun kinase pathway. *The Journal of biological chemistry* **293**, 20014-20028 (2018).

55. Boonekamp KE, *et al.* Identification of novel human Wnt target genes using adult endodermal tissue-derived organoids. *Dev Biol* **474**, 37-47 (2021).

56. Liu BC, *et al.* Global Transcriptional Analyses of the Wnt-Induced Development of Neural Stem Cells from Human Pluripotent Stem Cells. *International journal of molecular sciences* **22**, (2021).

57. Lee CS, Buttitta L, Fan CM. Evidence that the WNT-inducible growth arrest-specific gene 1 encodes an antagonist of sonic hedgehog signaling in the somite. *Proceedings*

*of the National Academy of Sciences of the United States of America* **98**, 11347-11352 (2001).

58. Yan W*, et al.* Epigenetic regulation of DACH1, a novel Wnt signaling component in colorectal cancer. *Epigenetics* **8**, 1373-1383 (2013).

59. Wang J*, et al.* DACH1 inhibits glioma invasion and tumor growth via the Wnt/catenin pathway. *Onco Targets Ther* **11**, 5853-5863 (2018).

60. Hu X*, et al.* Organoid modelling identifies that DACH1 functions as a tumour promoter in colorectal cancer by modulating BMP signalling. *EBioMedicine* **56**, 102800 (2020).

61. Shami Shah A*, et al.* PLEKHA4/kramer Attenuates Dishevelled Ubiquitination to Modulate Wnt and Planar Cell Polarity Signaling. *Cell reports* **27**, 2157-2170 e2158 (2019).

62. Park R, Lee S, Chin H, Nguyen AT, Lee D. Tumor-Promoting Role of GNA14 in Colon Cancer Development. *Cancers (Basel)* **15**, (2023).

63. Cervino AS, Moretti B, Stuckenholz C, Grecco HE, Davidson LA, Cirio MC. Furry is required for cell movements during gastrulation and functionally interacts with NDR1. *Scientific reports* **11**, 6607 (2021).

64. Emoto K*, et al.* Control of dendritic branching and tiling by the Tricornered-kinase/Furry signaling pathway in Drosophila sensory neurons. *Cell* **119**, 245-256 (2004).

65. Emoto K, Parrish JZ, Jan LY, Jan YN. The tumour suppressor Hippo acts with the NDR kinases in dendritic tiling and maintenance. *Nature* **443**, 210-213 (2006).

66. Fang X, Adler PN. Regulation of cell shape, wing hair initiation and the actin cytoskeleton by Trc/Fry and Wts/Mats complexes. *Dev Biol* **341**, 360-374 (2010).

67. Fang X, Lu Q, Emoto K, Adler PN. The Drosophila Fry protein interacts with Trc and is highly mobile in vivo. *BMC Dev Biol* **10**, 40 (2010).

68. He Y, Fang X, Emoto K, Jan YN, Adler PN. The tricornered Ser/Thr protein kinase is regulated by phosphorylation and interacts with furry during Drosophila wing hair development. *Molecular biology of the cell* **16**, 689-700 (2005).

69. Xiong S*, et al.* Structural Basis for Auto-Inhibition of the NDR1 Kinase Domain by an Atypically Long Activation Segment. *Structure* **26**, 1101-1115 e1106 (2018).

70. Stegert MR, Hergovich A, Tamaskovic R, Bichsel SJ, Hemmings BA. Regulation of NDR protein kinase by hydrophobic motif phosphorylation mediated by the mammalian Ste20-like kinase MST3. *Molecular and cellular biology* **25**, 11019-11029 (2005).

71. Hergovich A. The Roles of NDR Protein Kinases in Hippo Signalling. *Genes (Basel)* **7**, (2016).

72. Holehouse AS, Alberti S. Molecular determinants of condensate composition. *Molecular cell* **85**, 290-308 (2025).

73. Banani SF, Lee HO, Hyman AA, Rosen MK. Biomolecular condensates: organizers of cellular biochemistry. *Nat Rev Mol Cell Biol* **18**, 285-298 (2017).

74. Wang L*, et al.* Multiphase coalescence mediates Hippo pathway activation. *Cell* **185**, 4376-4393 e4318 (2022).

75. Bonello TT*, et al.* Phase separation of Hippo signalling complexes. *The EMBO journal* **42**, e112863 (2023).

76. Ludwig A. Selective Visualization of Caveolae by TEM Using APEX2. *Methods in molecular biology* **2169**, 1-10 (2020).

77. Martell JD, Deerinck TJ, Lam SS, Ellisman MH, Ting AY. Electron microscopy using the genetically encoded APEX2 tag in cultured mammalian cells. *Nat Protoc* **12**, 1792-1816 (2017).

78. Rybchyn MS*, et al.* Homer1 mediates CaSR-dependent activation of mTOR complex 2 and initiates a novel pathway for AKT-dependent beta-catenin stabilization in osteoblasts. *The Journal of biological chemistry* **294**, 16337-16350 (2019).

79. Cui X, Liang H, Hao C, Jing X. Homer1 is a Potential Biomarker for Prognosis in Human Colorectal Carcinoma, Possibly in Association with G3BP1 Signaling. *Cancer Manag Res* **12**, 2899-2909 (2020).

80. Liu Q*, et al.* HOMER3 facilitates growth factor-mediated beta-Catenin tyrosine phosphorylation and activation to promote metastasis in triple negative breast cancer. *J Hematol Oncol* **14**, 6 (2021).

81. Wang F*, et al.* ELK4 induced upregulation of HOMER3 promotes the proliferation and metastasis in glioma via Wnt/beta-catenin/EMT signaling pathway. *Biol Direct* **20**, 48 (2025).

82. Arnold A*, et al.* The majority of beta-catenin mutations in colorectal cancer is homozygous. *BMC cancer* **20**, 1038 (2020).

83. Jeon S, Jeon Y, Lim JY, Kim Y, Cha B, Kim W. Emerging regulatory mechanisms and functions of biomolecular condensates: implications for therapeutic targets. *Signal Transduct Target Ther* **10**, 4 (2025).

84. Schaefer KN, Peifer M. Wnt/Beta-Catenin Signaling Regulation and a Role for Biomolecular Condensates. *Dev Cell* **48**, 429-444 (2019).

85. Bienz M. Head-to-Tail Polymerization in the Assembly of Biomolecular Condensates. *Cell* **182**, 799-811 (2020).

86. Chen X, Jia B, Zhu S, Zhang M. Phase separation-mediated actin bundling by the postsynaptic density condensates. *eLife* **12**, (2023).

87. Zeng M*, et al.* Reconstituted Postsynaptic Density as a Molecular Platform for Understanding Synapse Formation and Plasticity. *Cell* **174**, 1172-1187 e1116 (2018).

88. Zhu S*, et al.* Demixing is a default process for biological condensates formed via phase separation. *Science* **384**, 920-928 (2024).

89. Ramsak M*, et al.* Programmable de novo designed coiled coil-mediated phase separation in mammalian cells. *Nat Commun* **14**, 7973 (2023).

90. Ramirez DA, Hough LE, Shirts MR. Coiled-coil domains are sufficient to drive liquid-liquid phase separation in protein models. *Biophysical journal* **123**, 703-717 (2024).

91. Singer A, Ramos A, Keating AE. Elaboration of the Homer1 recognition landscape reveals incomplete divergence of paralogous EVH1 domains. *Protein science : a publication of the Protein Society* **33**, e5094 (2024).

92. Hao S*, et al.* YAP condensates are highly organized hubs. *iScience* **27**, 109927 (2024).

93. Cai D*, et al.* Phase separation of YAP reorganizes genome topology for long-term YAP target gene expression. *Nature cell biology* **21**, 1578-1589 (2019).

94. Lu Y*, et al.* Phase separation of TAZ compartmentalizes the transcription machinery to promote gene expression. *Nature cell biology* **22**, 453-464 (2020).

95. Kiang KM, Ahad L, Zhong X, Lu QR. Biomolecular condensates: hubs of Hippo-YAP/TAZ signaling in cancer. *Trends Cell Biol* **34**, 566-577 (2024).

96. Zhao B*, et al.* Angiomotin is a novel Hippo pathway component that inhibits YAP oncoprotein. *Genes Dev* **25**, 51-63 (2011).

97. Paramasivam M, Sarkeshik A, Yates JR, 3rd, Fernandes MJ, McCollum D. Angiomotin family proteins are novel activators of the LATS2 kinase tumor suppressor. *Molecular biology of the cell* **22**, 3725-3733 (2011).

98. Liu X*, et al.* Tead and AP1 Coordinate Transcription and Motility. *Cell reports* **14**, 1169-1180 (2016).

99. Zanconato F*, et al.* Genome-wide association between YAP/TAZ/TEAD and AP-1 at enhancers drives oncogenic growth. *Nature cell biology* **17**, 1218-1227 (2015).

100. He L, Pratt H, Gao M, Wei F, Weng Z, Struhl K. YAP and TAZ are transcriptional co-activators of AP-1 proteins and STAT3 during breast cellular transformation. *eLife* **10**, (2021).

101. Ernkvist M, *et al.* The Amot/Patj/Syx signaling complex spatially controls RhoA GTPase activity in migrating endothelial cells. *Blood* **113**, 244-253 (2009).

102. Ludwig A. Protein droplets spread to seal tight junctions. *Nature* **632**, 506-507 (2024).

103. Wang L, *et al.* Overexpression of YAP and TAZ is an independent predictor of prognosis in colorectal cancer and related to the proliferation and metastasis of colon cancer cells. *PLoS One* **8**, e65539 (2013).

104. Cheung P, *et al.* Regenerative Reprogramming of the Intestinal Stem Cell State via Hippo Signaling Suppresses Metastatic Colorectal Cancer. *Cell stem cell* **27**, 590-604 e599 (2020).

105. Ou C, Sun Z, Li S, Li G, Li X, Ma J. Dual roles of yes-associated protein (YAP) in colorectal cancer. *Oncotarget* **8**, 75727-75741 (2017).

106. Planutis K, Planutiene M, Moyer MP, Nguyen AV, Perez CA, Holcombe RF. Regulation of norrin receptor frizzled-4 by Wnt2 in colon-derived cells. *BMC Cell Biol* **8**, 12 (2007).

107. Gupta S, *et al.* FZD4 as a mediator of ERG oncogene-induced WNT signaling and epithelial-to-mesenchymal transition in human prostate cancer cells. *Cancer research* **70**, 6735-6745 (2010).

108. Kim YH, *et al.* Hyaluronic acid synthase 2 promotes malignant phenotypes of colorectal cancer cells through transforming growth factor beta signaling. *Cancer science* **110**, 2226-2236 (2019).

109. Xuan Z, *et al.* NDR1/FBXO11 promotes phosphorylation-mediated ubiquitination of beta-catenin to suppress metastasis in prostate cancer. *International journal of biological sciences* **20**, 4957-4977 (2024).

110. Nong J, Kang K, Shi Q, Zhu X, Tao Q, Chen YG. Phase separation of Axin organizes the beta-catenin destruction complex. *The Journal of cell biology* **220**, (2021).

111. Schindelin J, *et al.* Fiji: an open-source platform for biological-image analysis. *Nature methods* **9**, 676-682 (2012).

## Figure 1: Homers localise to apical cell junctions in renal epithelial cells

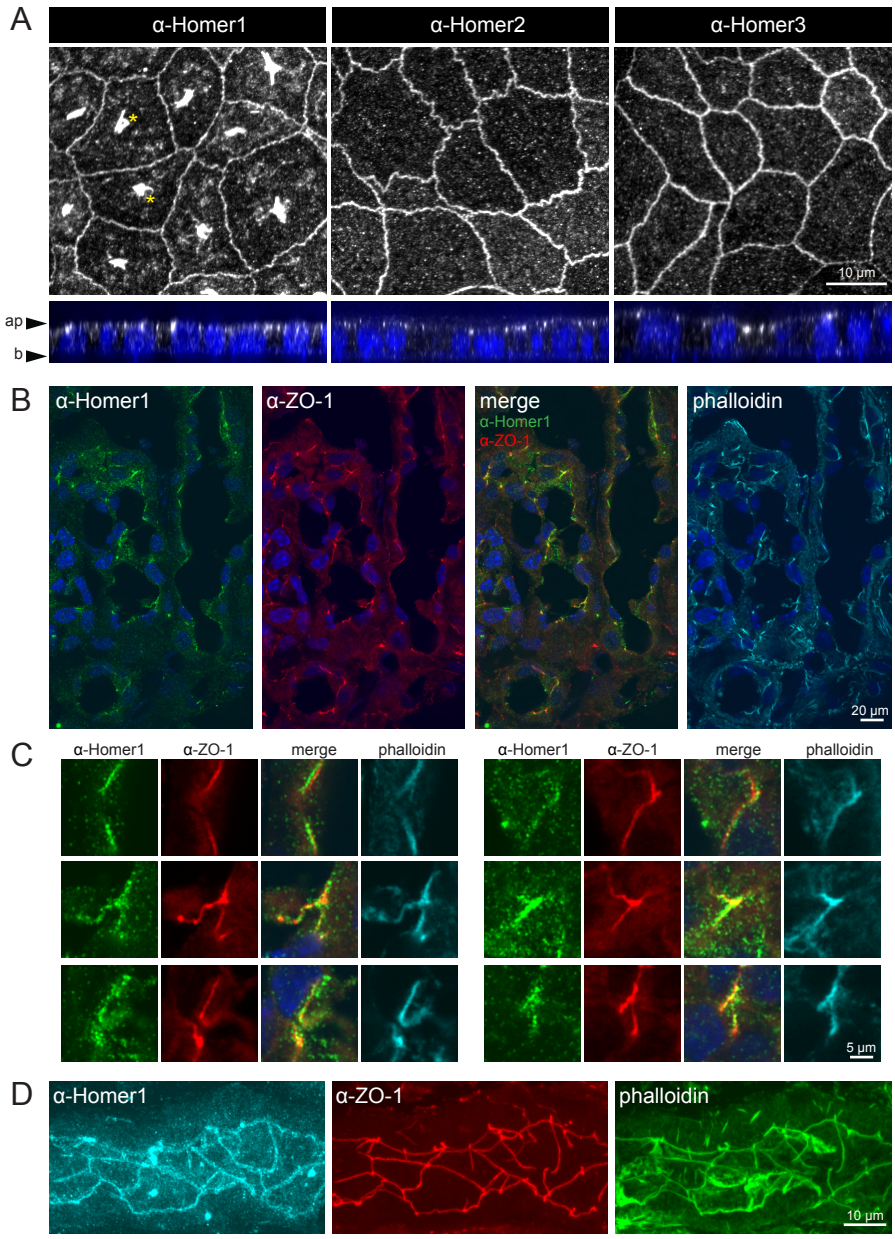

# Figure 2: Homers are recruited to apical cell junctions via a direct interaction with PatJ

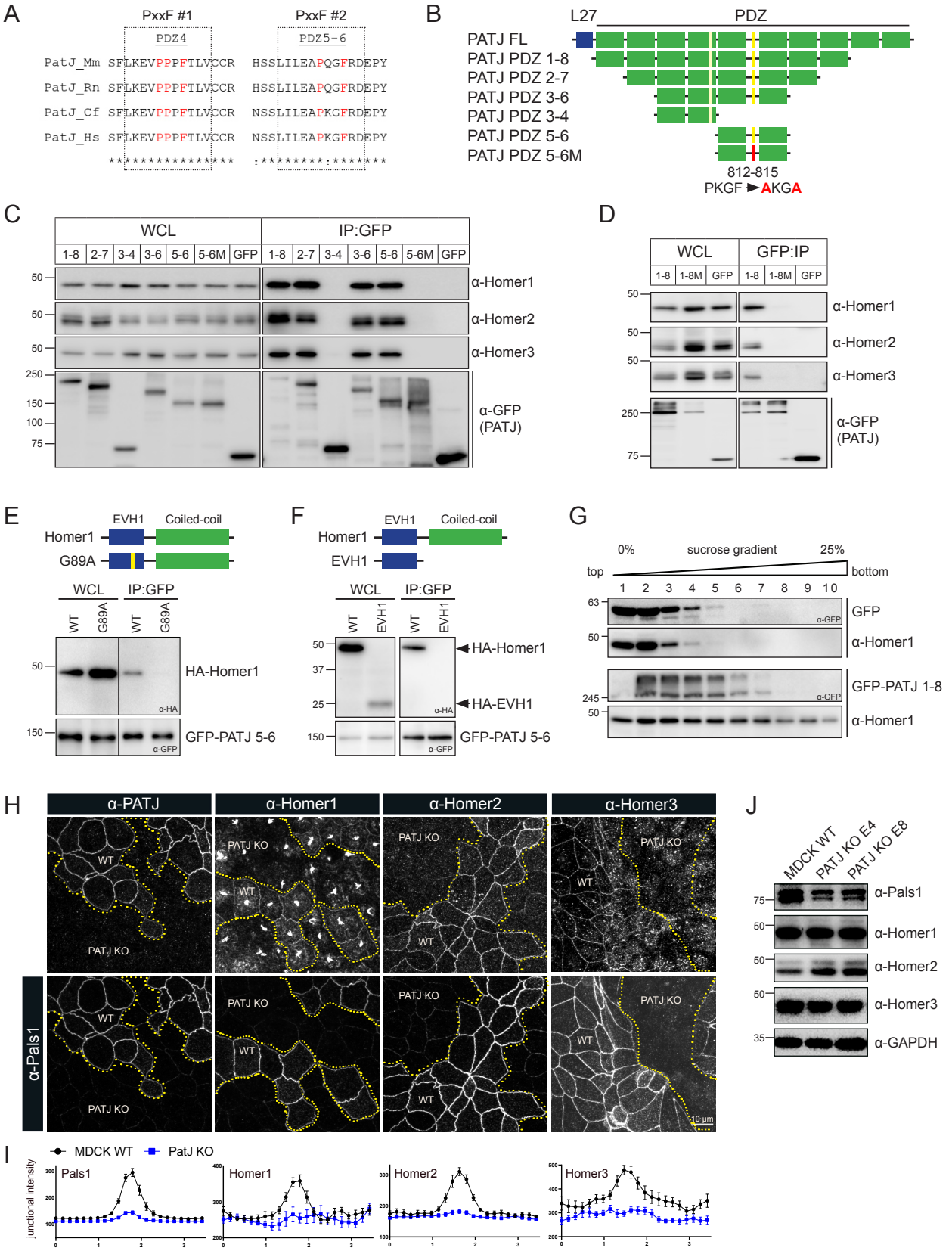

# Figure 3: Homers promote YAP and WNT signaling

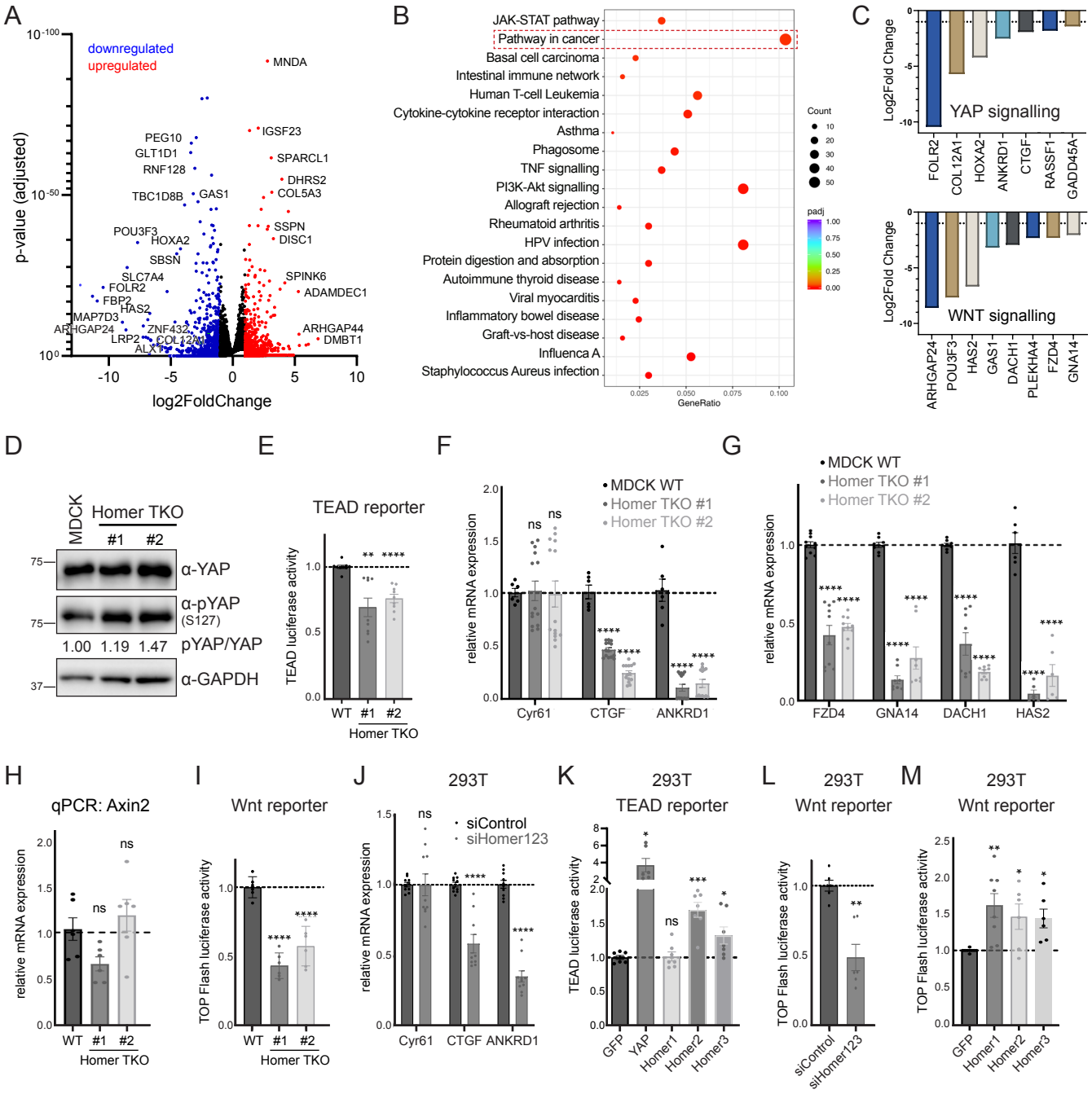

# Figure 4: The NDR kinase scaffolding protein FRYL interacts with Homers and suppresses YAP/TEAD signaling

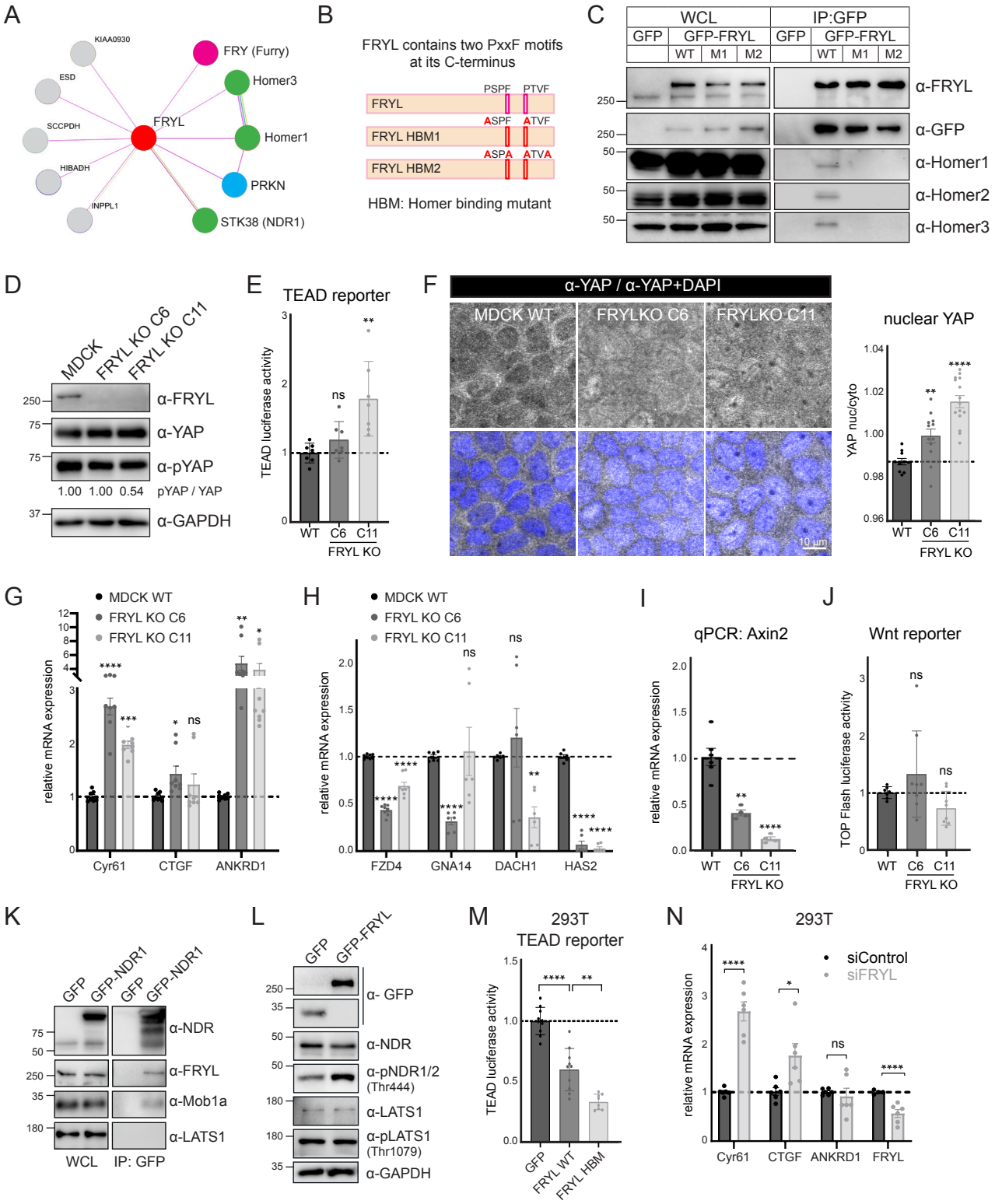

# Figure 5: Homers form cytoplasmic biomolecular condensates

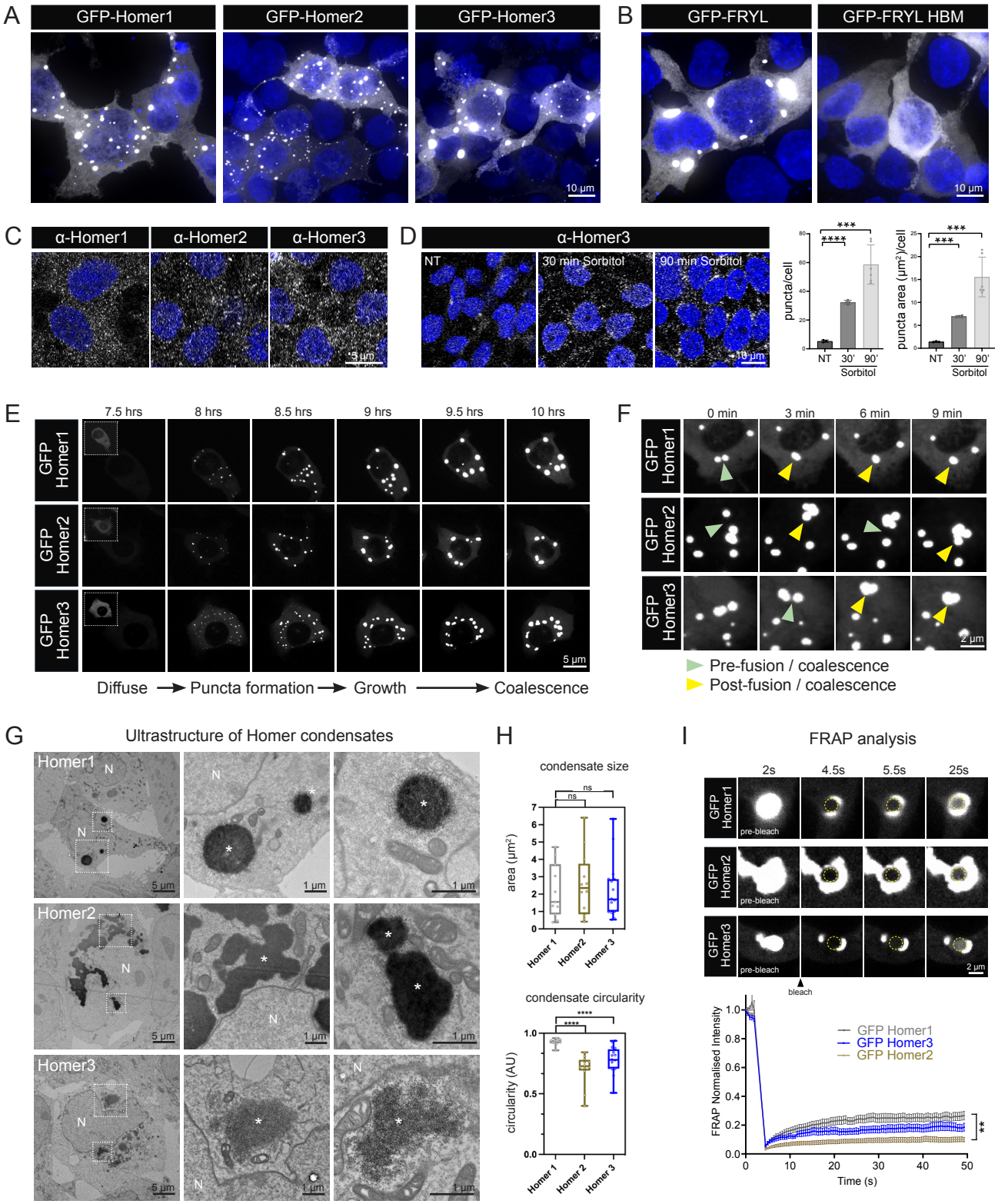

# Figure 6: Homers recruit FRYL, NDR, YAP and β-catenin into biomolecular condensates

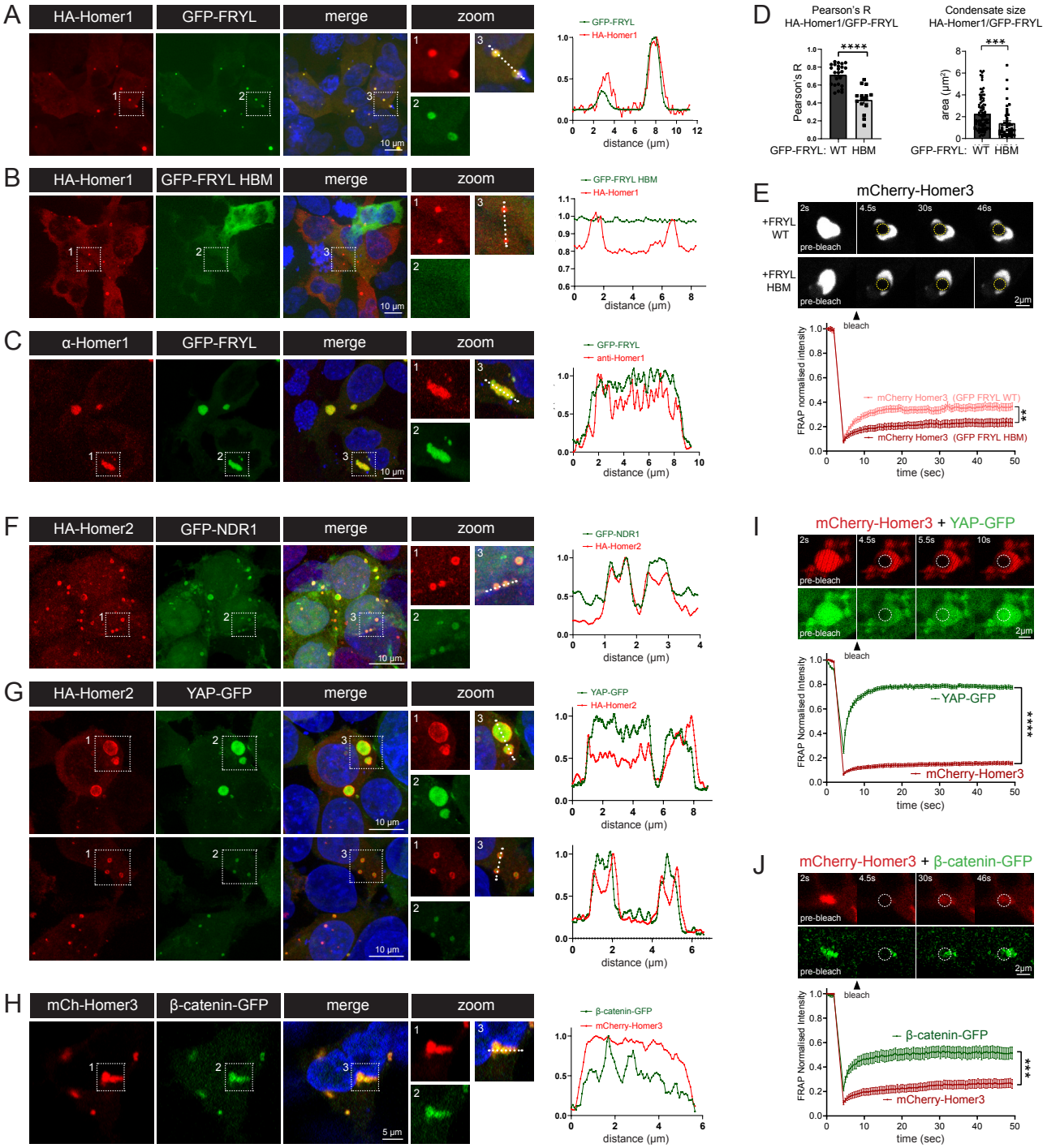

# Figure 7: PatJ regulates YAP and WNT signaling, in part via Homers

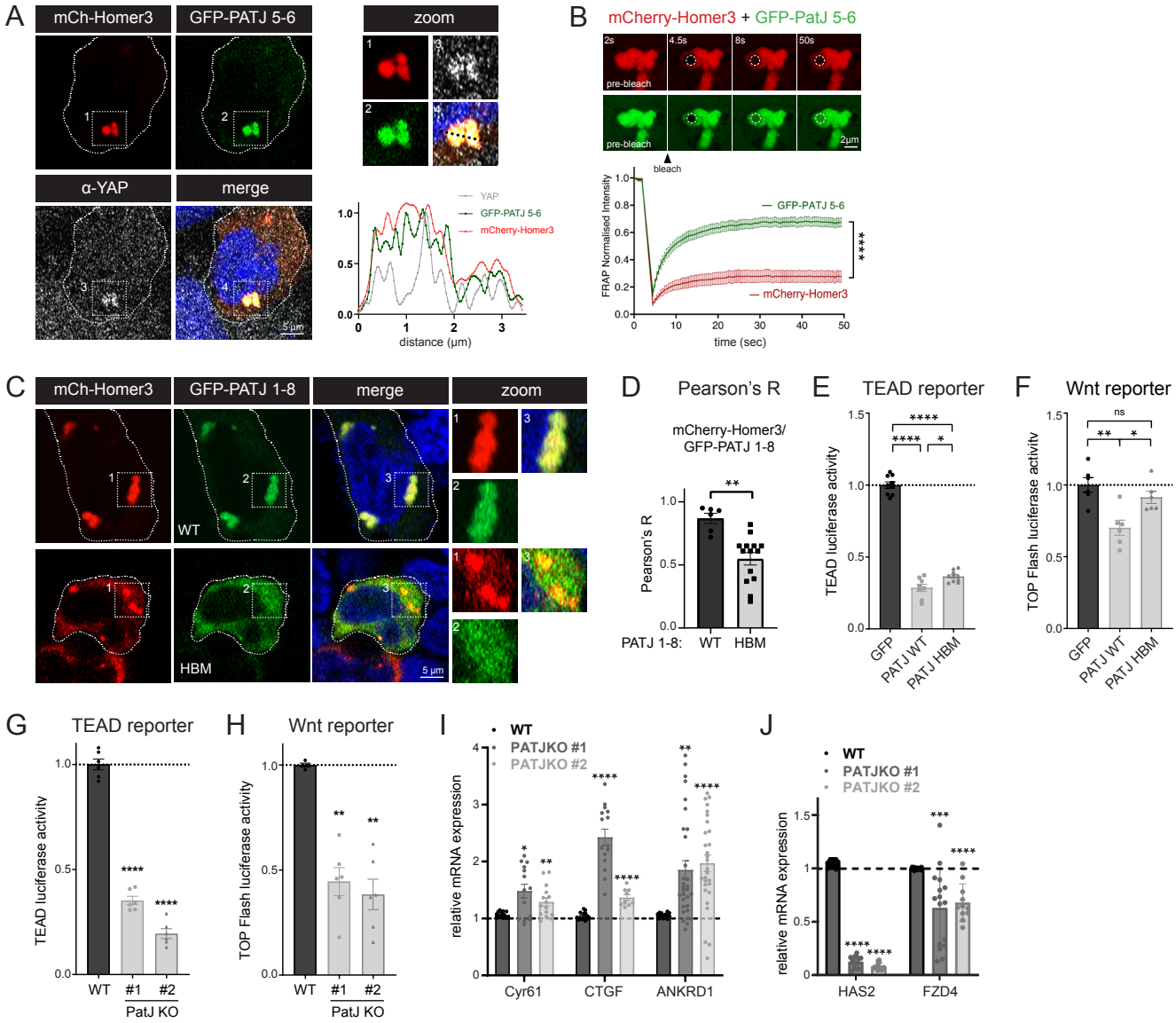

# Figure 8: Homers promote YAP/WNT signaling and migration in colorectal cancer cells

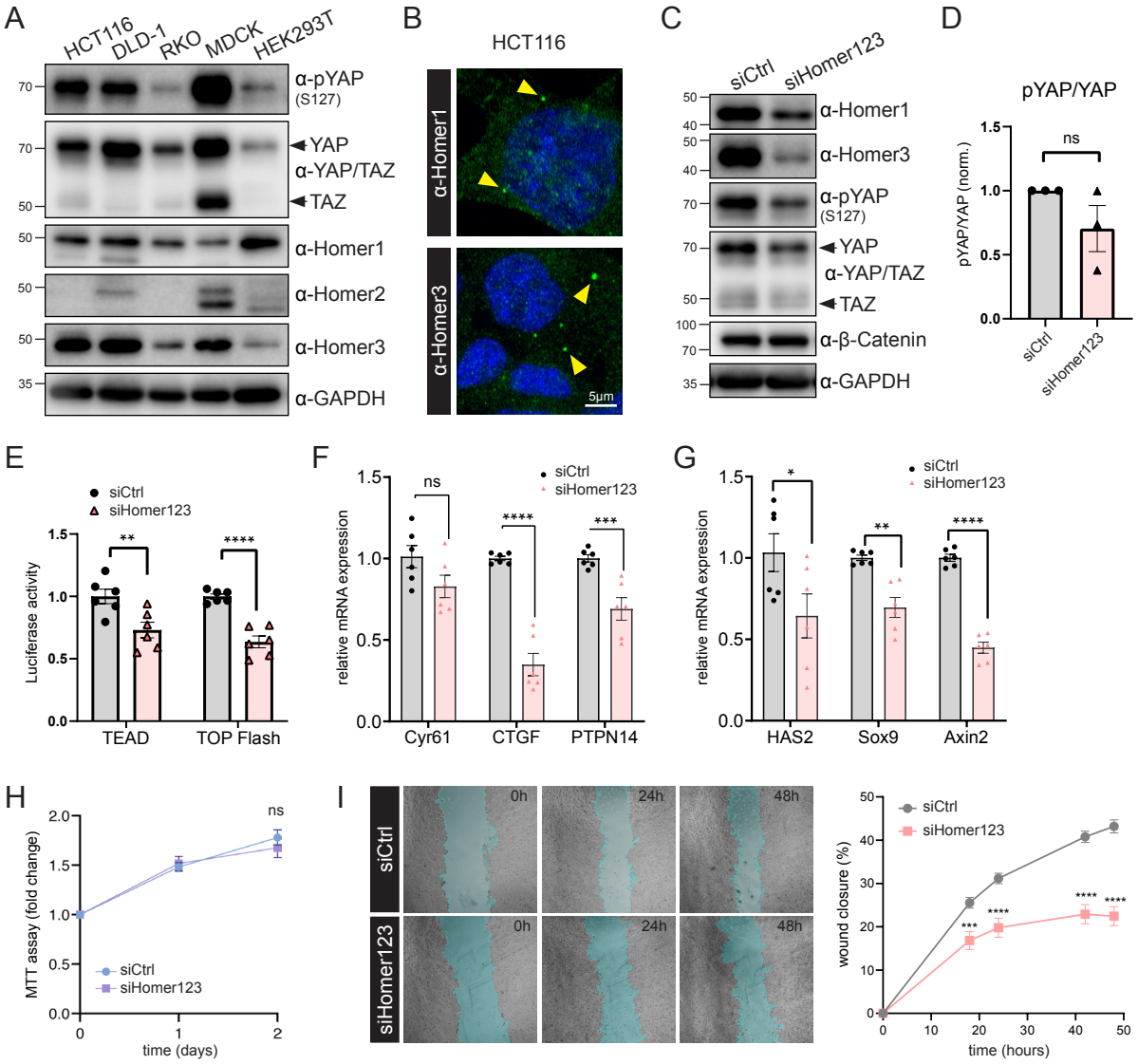
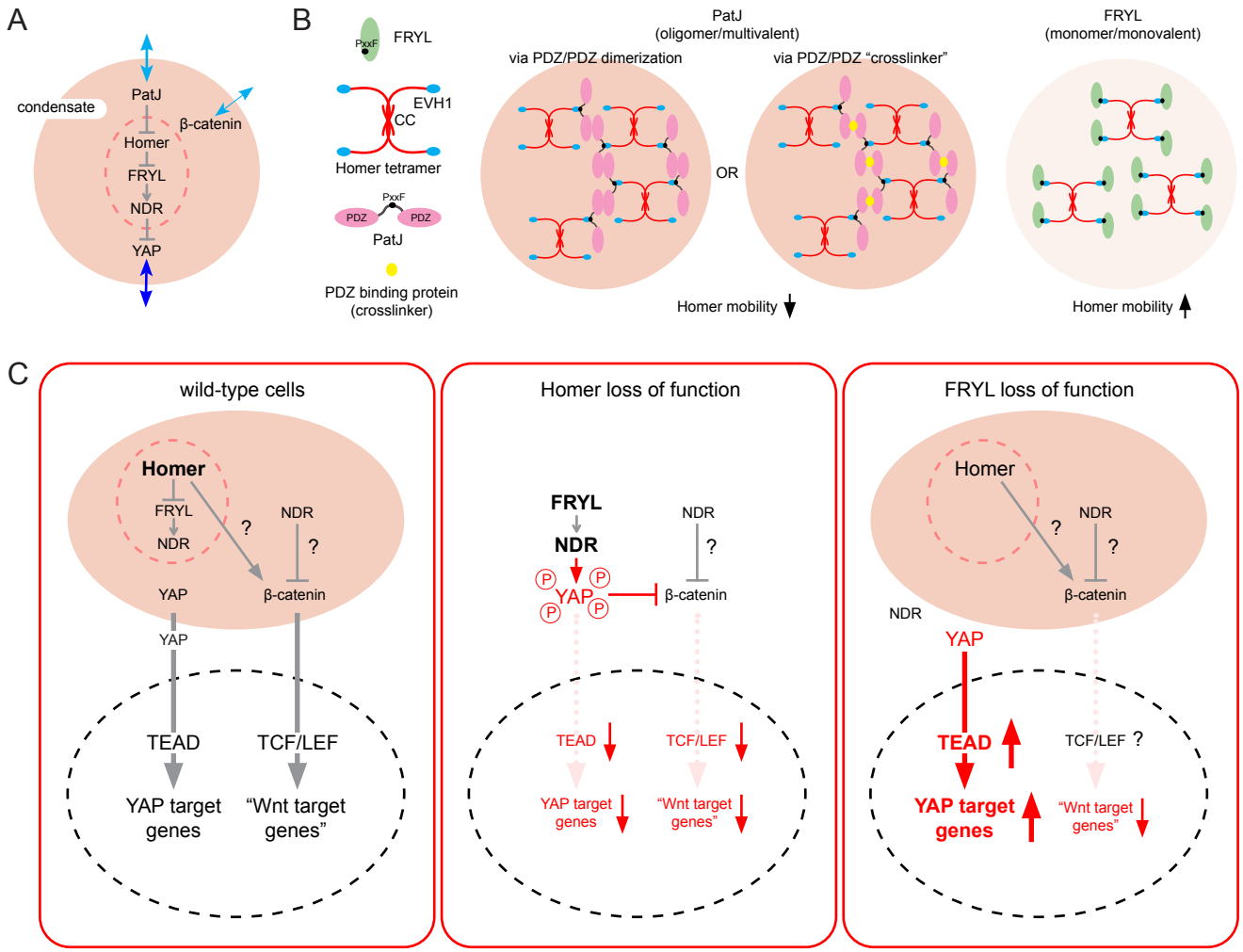
## Figure 9: Model of PatJ and FRYL function in Homer-dependent YAP/WNT signaling crosstalk